Formation of Igneous Layering in the Lower Oceanic Crust From the Samail Ophiolite, Sultanate of Oman

D. Mock[1,2] , **D. A. Neave**[1,3] , **S. Müller**[4] , **D. Garbe-Schönberg**[4], **O. Namur**[5] , **B. Ildefonse**[2] , and **J. Koepke**[1]

[1]Institut für Mineralogie, Leibniz Universität Hannover, Hanover, Germany, [2]Géosciences Montpellier, Université de Montpellier, CNRS, Université des Antilles, Montpellier, France, [3]Department of Earth and Environmental Sciences, The University of Manchester, Manchester, UK, [4]Institut für Geowissenschaften, Christian-Albrechts-Universität zu Kiel, Kiel, Germany, [5]Department of Earth and Environmental Sciences, KU Leuven, Leuven, KU, Belgium

Abstract As the largest and best exposed example of paleo fast-spreading oceanic crust on land, the Samail ophiolite in the Sultanate of Oman represents an ideal natural laboratory for investigating deep crustal processes at fast-spreading mid-ocean ridges. We studied two layered gabbro sequences from different stratigraphic depths: one from the middle of the plutonic crust showing decimeter-scale modal layering (i.e., varying phase proportions) with olivine abundances gradually decreasing from layer bases to tops (Wadi Somerah, Sumail block) and one located near the crust-mantle boundary showing millimeter-scale olivine-rich layers (Wadi Wariyah, Wadi Tayin block). Our multimethod approach of field, petrographic, geochemical, and microstructural observations focuses on documenting layered textures that are widely observed within the lower oceanic crust as well as understanding their formation mechanisms within the context of small scale crustal accretion processes beneath fast-spreading mid-ocean ridges. Results from the mid-crustal sequence indicate moderate cooling rates (Ca-in-olivine: $\log[\mathrm{d}T/\mathrm{d}t$; °C yr$^{-1}] = -2.21 \pm 0.7$) and correlated variations in mineral compositions and microstructures. We infer that decimeter-scale layers in Wadi Somerah were deposited by density currents of crystal-laden magma within a sill environment that potentially experienced occasional magma replenishment. The millimeter layering in Wadi Wariyah is best explained by Ostwald ripening emphasizing initial heterogeneities possibly being provoked by cyclical nucleation of olivine through the competing effects of element diffusion and rapid cooling. Fast cooling is recorded for the crustal base (Ca-in-olivine: $\log[\mathrm{d}T/\mathrm{d}t$; °C yr$^{-1}] = -1.19 \pm 0.5$, Mg-in-plagioclase: $\log[\mathrm{d}T/\mathrm{d}t$; °C yr$^{-1}] = -1.35$°C ± 0.6) demonstrating that heat locally can be lost very efficiently from the lowermost crust.

1. Introduction

Oceanic crust represents more than two thirds of Earth's surface. It is formed at mid-ocean ridges (MOR), where ~75% of Earth's volcanism takes place. The 60,000 km long global mid-ocean ridge system is the planet's most effective environment for exchanging mass and heat between interior of the Earth and the hydrosphere, which has major implications for global geochemical cycles. In spite of numerous ship-based sampling campaigns performed over recent decades aimed at investigating the modern oceanic crust, coherent sample series from the deep crust beneath fast-spreading ridges are rare. Therefore, it remains important to perform complementary studies on ophiolites, in particular on the Samail ophiolite in the Sultanate of Oman, which is regarded as the best example of fast-spreading oceanic crust on land. This ophiolite has played a pivotal role in developing crucial paradigms for understanding sea floor spreading and ocean crust formation (e.g., Boudier et al., 1996; France et al., 2009; Henstock et al., 1993; Kelemen et al., 1997; Nicolas et al., 2000; Pallister & Hopson, 1981; Phipps Morgan & Chen, 1993; Quick & Denlinger, 1993). Since modal layering is a ubiquitous feature of the lower crust, not only in Oman (e.g., Browning, 1984; Pallister & Hopson, 1981) but also at the recent East Pacific Rise (EPR; Gillis et al., 2014), its understanding is essential to approach the still unsolved question, how the crust accretes.

Many studies on ophiolite complexes performed in the 1980s and 1990s reported distinct rhythmic variations in modal proportions within the lower oceanic crust forming layered gabbros (e.g., Samail ophiolite in Oman, Troodos ophiolite on Cyprus, and Bay of Island ophiolite in Newfoundland; for a review see Nicolas, 1989). Their similarity to well-studied mafic layered intrusions, such as Bushveld (South Africa),

Skaergaard (Greenland), or Rum (Scotland), led to the hypothesis that cumulate formation and the layer-forming processes occurring during crustal accretion at mid-ocean ridges are similar to those taking place in layered intrusions.

Multichannel seismic experiments at the EPR in the late 1980s, however, ruled out the presence of large magma chambers of the kind implied by early models of ridge crust architecture (Detrick et al., 1987; Vera et al., 1990). Instead, these authors detected only small volume "chambers" about 100 m in height and <4–6 km in width at a crustal depth of 1.2–1.4 km (i.e., beneath the sheeted dyke complex) by their low seismic velocity. These have been interpreted as axial melt lenses (AMLs) residing on top of wider and thicker regions of anomalously low velocity material that have in turn been interpreted as partially molten crystal mushes and/or solidified (but still hot) plutonic sequences of the lower crust (e.g., Detrick et al., 1987; Vera et al., 1990).

Although many studies were performed in order to align these findings with crustal accretion models at fast-spreading ridges—without yet establishing a scientific consensus—only a few of them address the question of how layering formed within lower oceanic crust (e.g., Buck, 2000; Jousselin et al., 2012). In contrast, large continental layered intrusions are of scientific interest for many decades leading to numerous studies and detailed descriptions of different types of layering, that is, cyclic variations in textural, mineralogical, or chemical features of a rock. These variations can create grain size layering (e.g., Duke Island, USA; Irvine, 1974), textural layering (e.g., Rum Layered Suite, Scotland; Brown, 1956), cryptic layering (i.e., chemical variation; e.g., Skaergaard, Greenland; Wager & Brown, 1968; Sept Iles, Canada; Namur et al., 2010), or modal layering (i.e., variation in phase proportions) as it is observed in the lower oceanic crust. Layering varies in terms of layer thickness, regularity, or lateral continuity, and layer contacts can be sharp or gradational, or asymmetric. So far, there is only a consensus that no single process can account for all these types of layering but rather that many processes may play a role in creating different types of layering. Potential layer-forming processes have been described in several reviews (e.g., Namur et al., 2015; Naslund & McBirney, 1996) and can be divided into *dynamic* and *non-dynamic* processes. During dynamic processes, layering is formed within a magma chamber by movement of melt, mush, and/or crystals. This can include gravity-controlled settling, magma currents, convective-related processes, metasomatism, or magma replenishment and mixing. Non-dynamic layer-forming processes reflect conditional changes during crystallization or occur by self-organization of the mineral assemblage in a crystal mush. Layer formation by non-dynamic processes can include magmatic or tectonic deformation of a crystal mush, fluctuations of magma chamber conditions, diffusive exchange, or coarsening of grains.

The complexity of layer formation makes clear that both cumulus and post-cumulus processes have to be taken into account, especially when considering an oceanic spreading center where magmatic processes are continuously accompanied by tectonic and also hydrothermal processes. We approach this challenging situation by combining petrographic, petrological, geochemical, and microstructural data in order to constrain the layer-forming processes at different stratigraphic depths of the lower oceanic crust. As we point out in the next section, and as suggested by many groups before (e.g., Nicolas et al., 1988; Pallister & Hopson, 1981), we assume that the Oman ophiolite is a good analogue for recent fast-spread oceanic crust where, for example, modal layering was recently discovered by IODP Expedition 345 at Hess Deep (Gillis et al., 2014). Moreover, layered textures similar to those observed in the Oman ophiolite have also been found at Pito Deep at EPR (Gess et al., 2018; Perk et al., 2007). Understanding how layers form in the deep oceanic crust is thus crucial for constraining the dynamics and mechanisms of crustal accretion at fast-spreading ridges. Here we present observations on layered gabbros from two sites in the Samail ophiolite with contrasting modes of layer appearance, and we provide insights based on multi-method observations into the mechanisms that led to the formation of the studied layering.

2. Geological Setting

The Samail ophiolite in the Sultanate of Oman, a ~400 km long mountain chain of oceanic lithosphere obducted onto the Arabic continental margin during the Cretaceous, is regarded as the best example of fast-spreading oceanic crust on land (e.g., Nicolas et al., 2000). The mountain chain is located on the northeastern coast of Oman and covers an area of more than 20,000 km^2 (Pallister & Hopson, 1981). It is made up of twelve massifs that represent a complete crustal transect from the Moho transition zone (MTZ) via the

gabbros of the lower oceanic crust up to the volcanic layer consisting of sheeted dikes and erupted basalts. The paleo oceanic crust formed ~95 Ma ago (Rioux et al., 2013) and is thought to have formed at a fast-spreading center with a paleo half-spreading rate of 50–100 mm/yr (Rioux et al., 2012).

Geochemical investigations and field relations suggest a polygenetic origin for the Oman ophiolite (e.g., Alabaster et al., 1982; Goodenough et al., 2014; Koepke et al., 2009; Pearce et al., 1981; Yamasaki et al., 2006). A first phase produced the so-called V1 lavas and the majority of the gabbroic crust which is very similar to the modern EPR crust in terms of structure, lithology, petrography, and bulk crustal thickness. However, in contrast with the EPR, the parental basalts which formed the crust during the first magmatic stage in the Wadi Gideah (Oman) are thought to have contained elevated water contents of 0.4 to 0.8 wt% due to their formation in a subduction-influenced setting (MacLeod et al., 2013; Müller et al., 2017; Pearce et al., 1981). A second magmatic phase (V2) probably related to flux-induced peridotite melting subsequently intruded the first magmatic phase and consists of boninites in the upper crust and wehrlites, gabbronorites, and larger plagiogranite bodies in the lower and mid-crust (e.g., Goodenough et al., 2014; Juteau et al., 1988; Koepke et al., 2009; Yamasaki et al., 2006). The second magmatic stage is more voluminous in the northern blocks than in the southern segments of the ophiolite (e.g., Goodenough et al., 2014; MacLeod et al., 2013). Therefore, many studies that focused on understanding primary magmatic processes at mid-ocean ridges have been performed in the southern massif of the ophiolite (e.g., Garrido et al., 2001; Koga et al., 2001; VanTongeren et al., 2008).

In spite of the inferred location of the ophiolite in a region of subduction zone initiation, the following observations related to the first magmatic event demonstrate a close similarity with the modern, fast-spreading EPR: a continuous, typically layered crustal architecture with an average crustal thickness of 6–7 km (Lippard et al., 1986; Nicolas, 1989); an absence of amagmatic spreading that is common at slow-spreading ridges (e.g., Cannat & Casey, 1995); a very narrow range from 96.40 ± 0.17 to 94.18 ± 0.54 Ma of zircon crystallization ages across the width of the ophiolite (maximum ~100 km) sampled normal to the ridge direction (Rioux et al., 2012; Tilton et al., 1981; Warren et al., 2005); spinel Cr/Al versus Mg# (= MgO/(MgO + FeO); molar) ratios that overlap those for peridotites from modern fast-spreading ridges (Le Mee et al., 2004); the lengthscale of segmentation and absence of transform faults indicating a weaker impact of tectonic processes due to high magma supply (MacLeod & Rothery, 1992; Nicolas et al., 2000); and the orientation of a well-developed sheeted dike sequence perpendicular to the Moho which implies frequent magma ascent from the lower to the upper crust (MacLeod & Rothery, 1992). These features make clear that a detailed understanding of the magmatic processes which have formed the Oman paleo-crust provides insights into those taking place beneath recent fast-spreading centers. Our study focuses on outcrops in the southernmost blocks of the ophiolite at Wadi Somerah (Sumail block) and Wadi Wariyah (Wadi Tayin block), where the record of the second-stage magmatism is minor and comparisons with the modern EPR are well founded.

3. Materials and Methods

3.1. Sample Materials

We collected two types of samples from adjacent massifs of the Oman ophiolite (Sumail block for the material from Wadi Somerah, Wadi Tayin block for the material from Wadi Wariyah). They are consequently not representative of the same crustal section but were instead selected to represent two contrasting styles of layering. First, a suite of samples was taken from an outcrop in the central part of the layered gabbro section in the Wadi Somerah (N 23°5'34.66″, E 58°6'14.62″; Figure 1) that shows decimeter-scale modal layering (Figures 2a and 2b). This is representative of the average thickness of layering in the lower crust of the Oman ophiolite (Browning, 1984; Pallister & Hopson, 1981). The outcrop is about 30 m tall and 100 m wide. The modal layers are nearly horizontal at the southern face of the outcrop and can be followed over several tens of meters (Figure 2a). The layering is crossed by bright and dark centimeter-scale veins that usually propagate sub-perpendicular to the layering. As previously observed in Oman (e.g., Nicolas et al., 2000), olivine crystals are lineated. The much smaller western flank of the outcrop reveals the layering to be strongly sheared and folded (Figure 11a). We sampled a coherent profile of six consecutive layers. Each layer (except for layer 6 where we sampled only the layer base) consists of a melanocratic olivine-rich base that grades upsection into a leucocratic top that is significantly depleted in, or free from, olivine but strongly enriched
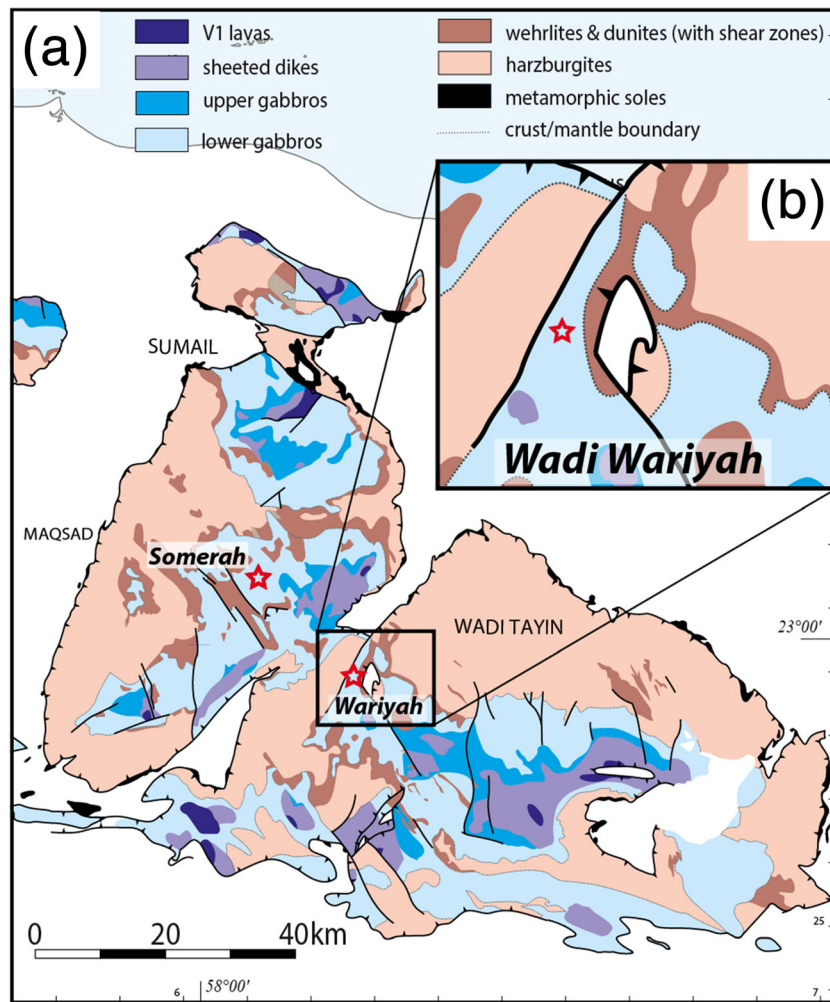
Figure 1. (a) Geological map of the southernmost massifs of the Oman ophiolite "Sumail" and "Wadi Tayin". (b) Crop of the geologically complex area of the Wadi Wariyah outcrop. The red stars give the positions of the two sampled outcrops in Wadi Somerah and in Wadi Wariyah. Map modified after Nicolas et al., 2000.

in plagioclase. Twenty-nine thin sections were prepared with a vertical distance of 1 to 42 cm between two stratigraphically successive samples.

Second, a single angular block was investigated which we collected just below an outcrop at the mouth of the Wadi Wariyah (N 22°59'0.42", E 58°15'54.68"; Figure 1). This outcrop represents deep layered gabbro at a crustal height of about 0.1 km above the MTZ (Bosch, 2004). The layering occurs as millimeter- or centimeter-thick layers with significantly differing olivine contents (Figure 2d). The locality where we collected the sample is located 300 m north to a well-studied outcrop of layered gabbro that preserves magmatic and hydrothermal veins ranging in formation temperature from very high (magmatic regime) to low temperatures which cut perpendicularly across the layering (Figure 2c; Bosch, 2004; Currin et al., 2018; Nicolas et al., 2003; Wolff, 2013). Foliation in plagioclase and olivine is here parallel to the igneous layering. Layering as thin as we observe in the investigated sample (millimeter-scale) has been rarely documented in the Oman ophiolite (Jousselin et al., 2012). Nonetheless, the analyzed sample allows new insights into magmatic processes operating in the lowermost oceanic crust. From this block, we prepared two thin sections that cover 111 coherent olivine-rich layers of the sample. Depth information given in the following chapters are estimated from the top of each sequence.

Although the sample from Wadi Wariyah originates from a locality with a complex geological evolution (Figure 1b), detailed mapping by Nicolas et al. (2000) and others (e.g., Bosch, 2004; Nicolas et al., 2003)
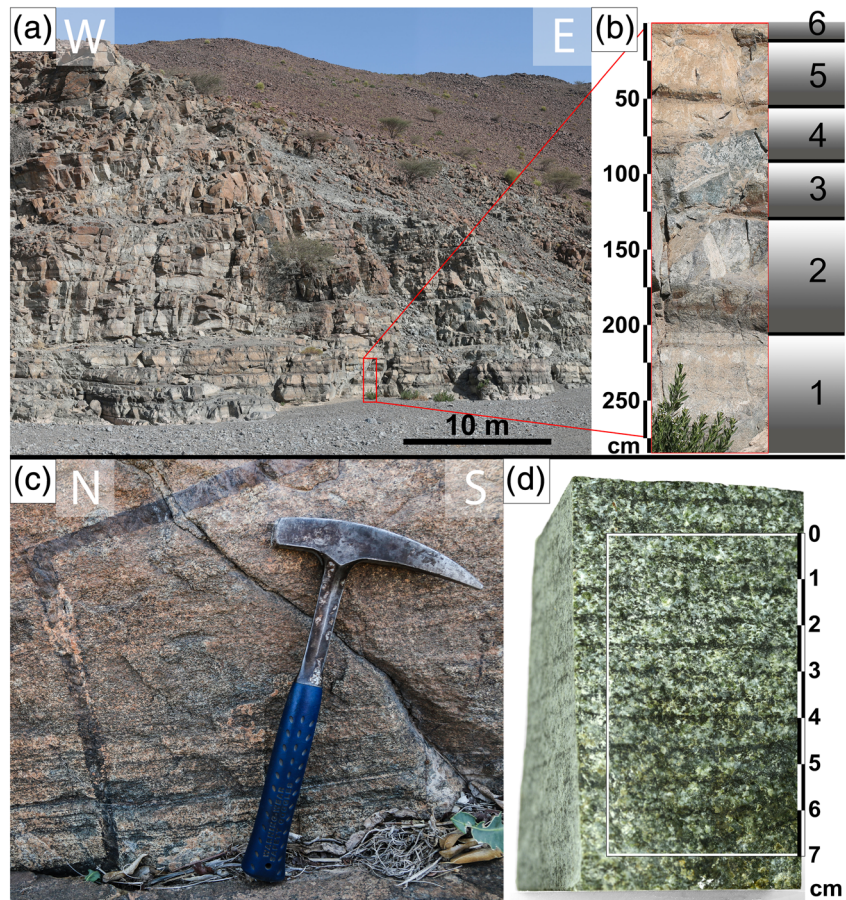
Figure 2. (a) Photograph of the outcrop in Wadi Somerah exposing decimeter-scale modal layering. (b) Shows the sequence sampled for this study, given by the red rectangle, in detail. Numbers 1–6 are the layer numbers, gray shaded fields represent melanocratic layer bases and leucocratic tops, demonstrating decreasing olivine content within each layer. Height of the sequence: 285 cm. (c) Photograph taken at an outcrop in Wadi Wariyah 300 m south of the locality where the sample in (d) was collected. It representatively shows millimeter-scale layering and a late stage magmatic vein perpendicularly cutting across the fine layering. Note the millimer-scale modal layering at the base and the gabbroic late-stage vein cross cutting the layered host rock. (d) Detailed photograph of the hand piece from the mouth of the Wadi Wariyah which was investigated in this study. Thin dark layers are olivine-rich. Rectangle symbolizes the region where two thin sections were prepared covering 11 layers. Note scale bars aside of B and D giving sequence heights in centimeters and which correspond to the depth intervals given in text and figures of this paper. Orientation directions given in white in (a) and (c). Photographs by D. Mock.

substantiates our interpretation that the sample originates from the lowermost layered gabbros close to the MTZ. Our samples were not collected as oriented samples. Therefore, we cannot comment on orientations of the measured foliations and lineations in a crustal context. Nevertheless, since thin sections from Wadi Wariyah have been prepared from the same piece of rock, the measured orientations are consistent along the profile. The samples from Wadi Somerah have been cut from one hand piece per melanocratic or leucocratic sub-layer, respectively, such that all thin sections of one sub-layer are oriented the same way providing consistency at the sub-layer scale.

3.2. Analytical Techniques

Petrographic analysis was performed using a binocular optical microscope. Modal proportions were estimated visually by comparison of thin section photographs with charts for estimating mineral percentages. Grain sizes have been measured along their long axis. The average grain size of a phase per thin section was calculated by measuring 10 grains: two of the smallest, two of the largest, and six medium-sized grains. Grains where chosen with respect to their habit, that is, poikilitic crystals were excluded from

measurement. With respect to best possible consistency along both sections, we decided to obtain phase proportions and grain sizes by visual estimation rather than EBSD analysis since the latter was for the Wadi Somerah only applied to a subset of samples. Nonetheless, we compared the results of our visual approach with those obtained by EBSD and found that both phase proportions and relative grain size differences between the samples are consistent between both methods.

Major and minor element compositions of olivine, clinopyroxene, and plagioclase were determined in the cores and rims of crystals in thin sections with a Cameca SX 100 electron microprobe at the Institute of Mineralogy in Hannover. The electron probe was operated through the *Peaksight* software. We used an accelerating voltage of 15 kV and a beam current of 15 nA. The beam was focused to 2 μm for olivine and plagioclase analyses; for clinopyroxene analysis the beam was defocused to 20 μm in order to integrate potential exsolution lamellae. Measurement times were 10 s on peak and 5 s on each background for all elements. Diffusion profile analyses of Ca in olivine were performed in order to estimate cooling rates (see below). For those analyses, we used a focused beam with an accelerating voltage of 15 kV and a beam current of 100 nA. Calcium was measured on a large pentaerythritol (LPET) crystal with a peak time of 240 s and 120 s on each background. High-precision analyses of Mg in plagioclase were also performed with an accelerating voltage of 15 kV and a high beam current of 100 nA. Magnesium was analyzed on a thallium acid phthalate (TAP) crystal with 240 s on peak and 120 s on each background. A matrix correction was applied following the PAP scheme (Pouchou & Pichoir, 1991).

In situ analyses of trace elements, and in particular of rare earth elements (REE), in plagioclase and clinopyroxene were performed at the Institute of Geosciences in Kiel using a 193 nm ArF excimer laser ablation system (GeoLasPro HD, Coherent) coupled to an Agilent 7,900-s inductively coupled plasma mass spectrometry (ICP-MS). Analyses were performed as point measurements with 16 Hz pulse rate, 18 Jcm^{-2} fluence, and a crater diameter of 120 μm on plagioclase, and 10 Hz, 12 Jcm^{-2}, and a crater diameter of 32 μm on clinopyroxene. Helium was used as carrier gas with addition of 14 ml H$_2$. Initial data processing and setting of integration intervals were performed with the GLITTER software package, applying the method of internal standardization with CaO as determined from electron probe measurements as internal standard and using NIST SRM612 for initial calibration. A second matrix matched calibration step was applied using micro-analytical reference materials BIR-1P, BHVO-2P, JGb-1P, and JF-1P prepared as nano-particulate pellets (Garbe-Schonberg & Muller, 2014; see calibration data in Mock et al., 2020b). Precision of replicate measurements was <2% relative standard deviation for most elements with an accuracy of ~5% RMSD (root-mean-square deviation) on BCR-2G at >10*LOD (limit of detection; see accuracy data in Mock et al., 2020b).

Electron backscatter diffraction (EBSD) mapping was performed at Géosciences Montpellier with a JEOL JSM 5600 scanning electron microscope equipped with an Oxford/Nordlys EBSD detector and using the *Aztec* software. We used an accelerating voltage of 15 kV. Analyses were performed for each crystal along a grid with a step size of 16.5 to 30.0 μm depending on grain size.

3.3. Estimation of Cooling Rates and Crystallization Temperatures

Cooling rates were estimated using the Ca-in-olivine speedometer (Coogan et al., 2005) and the Mg-in-plagioclase speedometer (Faak et al., 2014). Both methods use diffusion profiles in crystals to estimate how fast the rocks cooled in the sub-solidus down to their closure temperatures. Following the arguments of Coogan et al. (2007), we modeled the Ca diffusion in olivine at a fixed fO_2 of 10^{-12} bar. Both methods, Ca-in-olivine and Mg-in-plagioclase, are based on high spatial resolution rim-core-rim electron microprobe profiles in olivine or plagioclase crystals, respectively, that are adjacent to clinopyroxene crystals which serve as semi-infinite reservoirs for both Ca and Mg. Using the geothermometers of Shejwalkar and Coogan (2013) for Ca-in-olivine and Faak et al. (2013) for Mg-in-plagioclase allows the closure temperature (T_c)—the temperature at which diffusion in the crystal becomes too inefficient for significant changes in element distribution to occur—to be estimated for every measurement point along a rim-core-rim profile. T_c depends on the distance from the interface (Dodson, 1986; Onorato et al., 1981) such that the shape of profile, that is, the absolute values for T_c and the relative difference between core and rim data, can be used to estimate the sub-solidus cooling rate.

Modeling diffusion profiles and using them for geospeedometry involves several sources of uncertainty which we tried to minimize or eliminate. As shown by Dalton and Lane (1996), rim analyses of Ca as a

trace element in olivine adjacent to a Ca-rich phase are highly sensitive to secondary fluorescence. The profiles started and ended always ~5 µm from the rim. Following Coogan et al. (2002), secondary fluorescence potentially affects the outermost 100 µm of a profile. However, the profiles used for the modeling have very similar shapes with only small differences between core and rim composition, regardless of the adjacent phases at the start and end of the profile. Since we would expect secondary fluorescence to affect every profile in a different way (i.e., depending on adjacent phases; Coogan et al., 2002), the similarities between the profiles appear unlikely to result from secondary fluorescence. Moreover, taking the small number of clear outliers in the measured profiles on many different samples into account, it is improbable that secondary fluorescence significantly affected our results. Uncertainties may also arise from grain shapes (i.e., cutting effects; e.g., Coogan et al., 2007) which we tried to minimize by analyses of several grains per sample. Occasionally, we performed measurements of two perpendicular profiles per grain in order to eliminate erroneous impact from crystal shapes. The similarity of results obtained by applying independent methods (i.e., Ca-in-olivine and Mg-in-plagioclase) in Wadi Wariyah suggests that both methods are reliable. All profile data are collected in Mock et al. (2020a). Crystallization temperatures were estimated using the thermometer of Sun and Liang (2017) that exploits the temperature-dependent partitioning of REE between plagioclase and clinopyroxene.

3.4. Processing EBSD Data

The first steps of post-processing and refining EBSD data were performed with the *Channel5* Tango application. Grain statistics, maps, eigenvalue analyses, and pole figures were calculated using the MTEX toolbox for Matlab® (e.g., Mainprice et al., 2015). Very small grains with a size of less than 10 pixels were deleted since they are assumed to be results of analytical errors. Twins in plagioclase and clinopyroxene were defined assuming a misorientation angle of 180° ± 2 to the neighbored grain of the same phase. Crystallographic preferred orientations (CPO) were quantified using the J index of the orientation distribution function (called ODF J index here) after Bunge and Esling (1982), which varies between 1 for a random fabric and ∞ for a single crystal. The pole figure symmetry was quantified using the BA index for plagioclase and the BC indices for clinopyroxene and olivine, respectively (Satsukawa et al., 2013). These indices vary between 0 for a foliated symmetry (axial B-type) and 1 for a lineated symmetry (axial A-type or axial C-type, respectively). The intermediate P-type symmetry corresponds to an index of ~0.5. Using the orientation of each pixel, it is possible to calculate the misorientation of a single pixel from the average orientation of the corresponding grain and, therefore, to quantify the internal misorientation of a grain. The grain orientation spread (GOS) is the average internal misorientation of all grains per phase in a sample. Hence, the GOS provides a quantification of the intracrystalline deformation intensity per mineral phase within the samples. We present and interpret the GOS for plagioclase and clinopyroxene only. Due to intense mesh serpentinization, olivine grain boundaries obtained by EBSD were determined incorrectly, meaning that the GOS cannot be calculated for whole primary grains and is therefore probably underestimated. Pole figures and fabric indices of plagioclase and clinopyroxene were calculated using a randomly chosen pixel per grain (grain data) instead of all indexed pixels (grid data; e.g., Satsukawa et al., 2013) in order to avoid that data from large grains become overestimated. Due to the potentially incorrect identification of olivine grain boundaries, olivine fabrics have been calculated using the grid data. This may lead to an increased ODF J index.

4. Results

4.1. Wadi Somerah

The primary lithologies of the decimeter-scale layering in Wadi Somerah are gabbros or olivine gabbros with the main phases being plagioclase, clinopyroxene, and olivine. Modal layering is mostly expressed by variability in olivine contents of up to 23% in melanocratic layer bases and less than 10% in leucocratic tops (Figure 4). Complex mesh serpentinization of olivine leads to the dark appearance of the layer bases observed in the field. Olivine-enriched layer bases and olivine-depleted layer tops are represented by EBSD phase maps in Figures 3a and 3b. Plagioclase usually forms the smallest grains with grain sizes of 0.2–0.7 mm long axis length. Olivine and clinopyroxene grain sizes are larger, with average grain sizes of 1–2.5 mm. Clinopyroxene grains are the largest at the base of layer 2, which has significantly larger grains than the top of layer 1 (see layer details in Figure 4). An increasing trend in grain size toward the layer base is only observed in layers 1 and 2; other layers show either no trend or even a trend of grain size coarsening
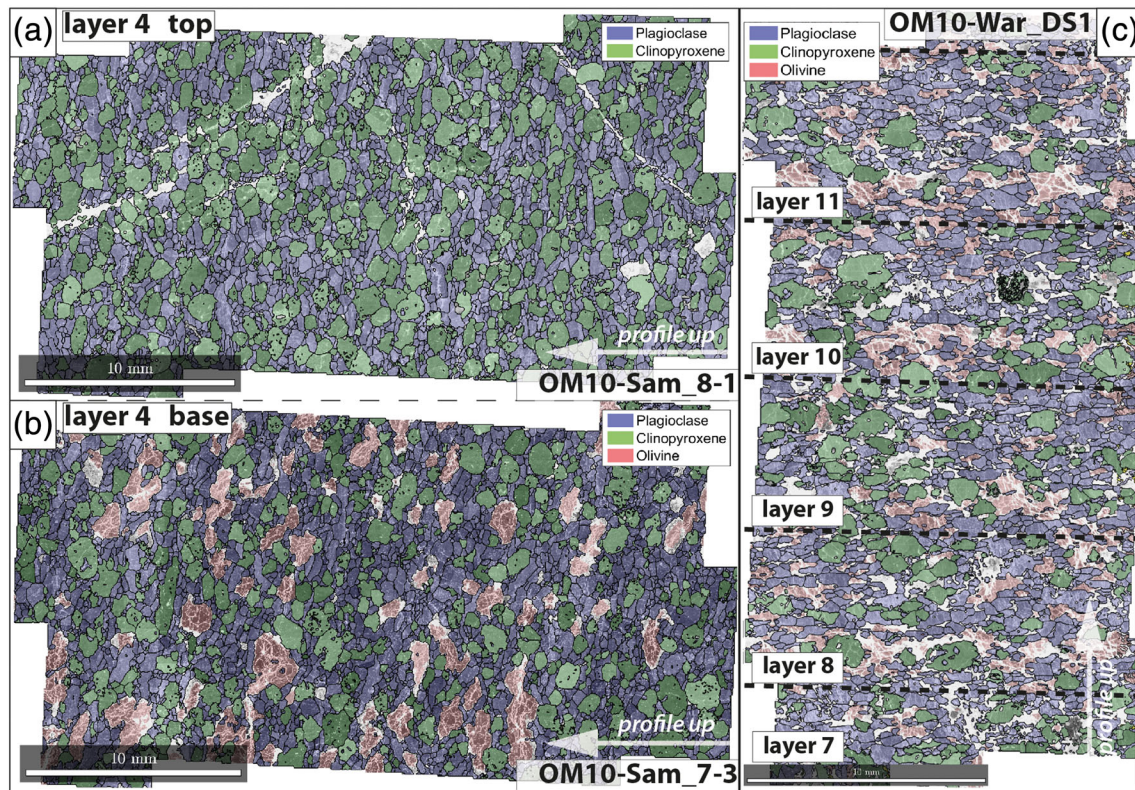
Figure 3. Phase maps of three thin-sections from our study. (a) Sample OM10-Sam_8-1 representing the leucocratic, olivine-poor top of layer 4. (b) Sample OM10-Sam_7-3 representing the melanocratic, olivine-rich base of layer 4. Both (a) and (b) correspond to the decimeter-scaled layering in Wadi Somerah. (c) Sample OM10-War_DS1 covering layers 1–5 from the millimeter layering in Wadi Wariyah. Note the legend of every image. The bars at the image bases are 10 mm. White arrows give direction profile up.

upward. On a thin-section scale, grain size variation is small for every phase (see representative phase maps in Figures 3a and 3b). The grain shape of all phases is anhedral to subhedral with prismatic and occasionally elongated habits. Plagioclase occasionally forms chadacrysts in poikilitic clinopyroxene or olivine, indicating that plagioclase partially crystallized simultaneously with olivine and clinopyroxene. Olivine shows strong alteration to mesh serpentine, often related to alteration veins and their halos, implying that olivine alteration was triggered by hydrothermal activity. An alignment of elongated olivine crystals is well preserved in leucocratic samples with small amounts of olivine. The majority of olivine grains in the melanocratic samples shows a round shape and no clear lineation. All petrographic results are summarized in Table 1.

Mineral compositions (see Mock et al., 2020a, for compositional data) from the Wadi Somerah sequence show that there is no general correlation with position in different modal layers (Figure 4). The core Mg# ($[Mg/(Mg + Fe)] \times 100$; molar basis) in olivine varies between 78.1 and 80.6. From the base of the sequence up section, the Mg# is nearly constant in the depth interval between 225 and 275 cm. It significantly decreases from 80.5 to 78 toward the base of layer 2 at a depth in the sequence of 200 cm. Above this minimum, the Mg# increases up section to 175 cm, reaching its maximum of 80.6. The following trend up section is relatively homogeneous, showing a slight decrease which is most pronounced between the base and top of layer 5. NiO in olivine follows the Mg# trend of olivine except for layer 2 and layer 5, where NiO is decoupled from the Mg# value.

The Mg# in clinopyroxene cores shows nearly constant values throughout the stratigraphy with only limited variability between 83.7 and 85.9, showing small shifts within the natural variability along the whole sequence. These shifts seem not to correlate with the Mg# in olivine. The most distinct shift in clinopyroxene Mg# occurs in layer 5, where it varies from 84 to 85.8 in a single sample, while the corresponding olivine in
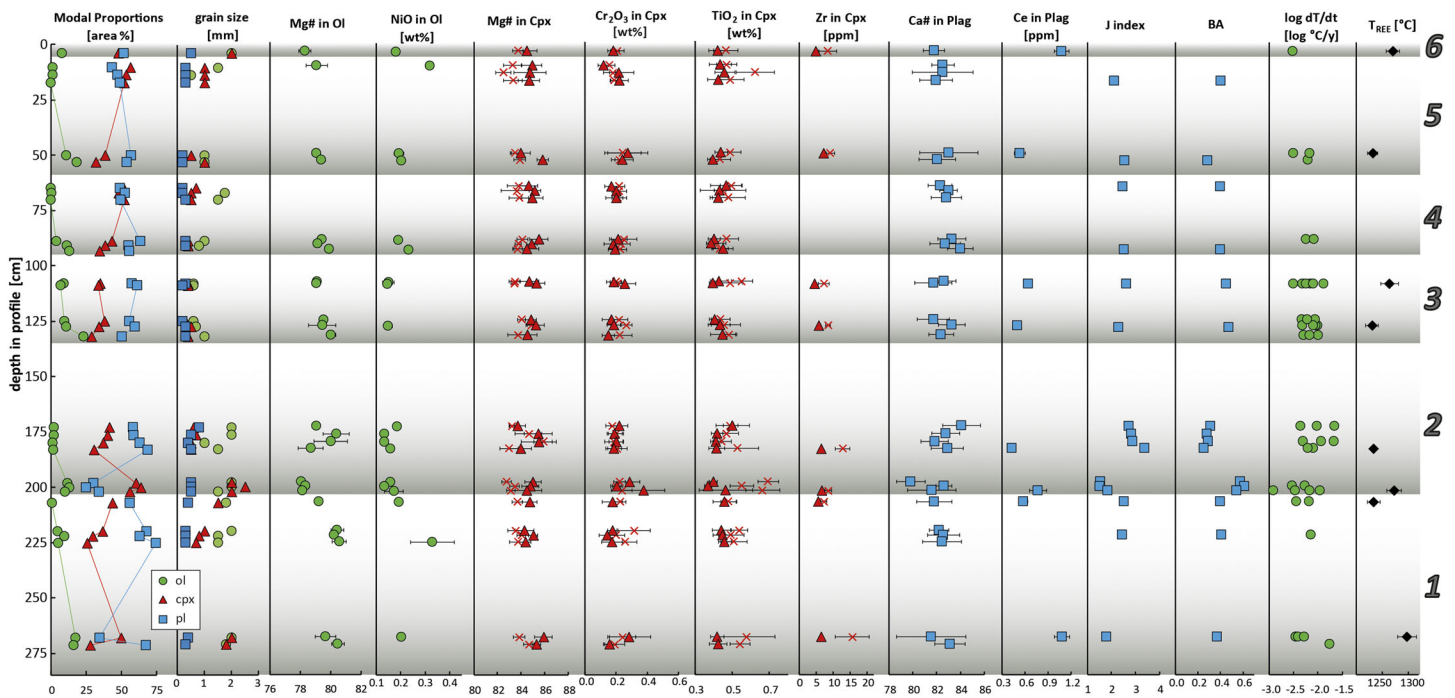
Figure 4. Summarized results of analyses on the decimeter-scale layered gabbro sequence from Wadi Somerah. Gray numbers on the right give the layer number; gradational gray background symbolizes the layer color, most pronounced by olivine content. Closed symbols are core; crosses are rim analyses. Black bars in element plots give 1 sigma standard deviation from the mean. Black bars in T_{REE} plot give standard error of the regression line provided by the Sun and Liang (2017) excel sheet. Mg# = Mg/(Mg + Fe)x100; molar basis, Ca# = Ca/(Ca + Na)x100; molar basis. Note correlating trends with respect to several data sets within a given layer, most pronounced in layer 2. See text for further interpretation.

the same horizon does not show this anomaly to more primitive compositions, neither with respect to the Mg# nor to NiO. In contrast to olivine and plagioclase, clinopyroxene crystals are slightly zoned, with higher Mg# values in the core. Rim Mg#s generally vary between 81.8 and 85.9. The degree of zoning differs significantly (up to 2 Mg# units between core and rim at the base of layer 2) but does not show any evolution in the whole sequence or within individual layers. We also observed zoning in TiO_2 with concentrations being increased in the rims by an average enrichment factor of 1.18 (with 1.74 at maximum). Incompatible trace elements (represented by Zr in Figure 4) reflect this trend consistently, with higher values in the rims enriched by a factor of up to 2.4 in the case of Zr. All trace element data are collected in Mock et al. (2020b).

Ca# ([Ca/(Ca + Na)] × 100, molar basis) in plagioclase covers a range between 79.8 and 84.1 with a distinct minimum at a depth of 200 cm (base of layer 2), clearly correlating with the minimum in Mg# of olivine in that horizon. The Ca# increases above and below this point from 79.8 to 82.9 and 82.6, respectively. The evolution of the Ce content (representing a proxy for plagioclase trace element content) inversely correlates with the trends of the Ca# within layers 2 and 3 (i.e., increasing Ce with decreasing Ca# and vice versa) but behaves differently within layer 1 and at the transition between layers 5 and 6 where Ce shows a considerable scattering at constant Ca#.

A high spatial resolution microprobe profile with a step size of 27 μm throughout the transition between layer1 and layer 2 reveals slight differences in clinopyroxene composition, indicating that clinopyroxene at the base of layer 2 is more primitive than at the top of layer 1 (Figure 5). The profile also reveals a slightly lower Mg# in olivine, which is consistent with core and rim analyses but does not fit the observed difference of more primitive clinopyroxene composition in layer 2. In contrast, the mean plagioclase Ca# is similar in both layers but shows significant intergranular heterogeneities.

Crystallization temperatures estimated using the Sun and Liang (2017) REE-in-plagioclase-and-clinopyroxene thermometer range between 1230°C and 1300°C, with a mean of 1254°C and a one sigma standard

Table 1
Petrographic Observations and Phase Properties for Sample Sets From Wadi Somerah (OM10-Sam) and Wadi Wariyah (OM10-War)

Sample	DiS (cm)[a]	Lithology[b]	Grain size mode[c]	Olivine Mode (%)[d]	Olivine GS (mm)[e]	Olivine Shape[f]	Olivine Habit[g]	Olivine Comment[h]	Plagioclase Mode (%)[d]	Plagioclase GS (mm)[e]	Plagioclase Shape[f]	Plagioclase Habit[g]	Plagioclase Comment[h]	Clinopyroxene Mode (%)[d]	Clinopyroxene GS (mm)[e]	Clinopyroxene Shape[f]	Clinopyroxene Habit[g]	Clinopyroxene Comment[h]
OM10-Sam_11	4	ol gb	med	7	2.0	shd	prm	oc, rrm	48	0.5	shd	elg	cc	45	2.0	shd	prm	oc
OM10-Sam_10-1	10.5	ol-b gb	fin	1	1.5	shd	prm	oc, rrm	43	0.3	shd	elg	cc	56	1.0	shd	prm	oc
OM10-Sam_10-2	13.85	ol-b gb	fin	1	0.5	shd	prm	oc, rrm	47	0.3	shd	elg	cc	52	1.0	shd	prm	oc
OM10-Sam_10-3	17.35	gb	fin			—			49	0.3	shd	elg	cc	51	1.0	shd	prm	oc
OM10-Sam_9-1	49.95	ol gb	fin	10	1.0	shd	prm	oc, rrm	54	0.2	shd	elg	cc	36	0.5	shd	prm	oc
OM10-Sam_9-2	53.05	ol gb	fin	18	1.0	shd	prm	oc, rrm	52	0.2	shd	elg	cc	30	1.0	shd	prm	oc
OM10-Sam_8-1	64.9	gb	fin			—			49	0.2	shd	elg	cc	51	0.7	shd	prm	oc
OM10-Sam_8-2	67.1	ol-b gb	fin	1	1.8	shd	prm	rrm	52	0.2	shd	elg	cc	47	0.5	shd	prm	oc
OM10-Sam_8-3	70.2	ol-b gb	fin	1	1.5	shd	prm		49	0.3	shd	elg	cc	50	0.5	shd	prm, elg	oic
OM10-Sam_7-1	88.9	ol gb	med	3	1.0	shd	prm, elg		57	0.3	shd	elg, prm	cc	40	0.4	shd	prm	oc
OM10-Sam_7-2	90.95	ol gb	med	11	0.8	shd	prm	rrm	52	0.3	shd	elg, prm	cc	37	0.4	shd	prm, elg	oc
OM10-Sam_7-3	93.4	ol gb	med	13	0.6	shd	prm, elg	rrm	53	0.3	shd	elg, prm	cc	34	0.4	shd	prm	oc
OM10-Sam_6-1	107.9	ol gb	med	9	0.6	shd	prm, elg	rrm	57	0.3	shd	elg	cc	34	0.4	shd	prm	oc
OM10-Sam_6-2	108.7	ol gb	med	7	0.6	shd	prm	rrm	60	0.2	shd	prm, elg	cc	33	0.4	shd	prm, elg	oc
OM10-Sam_5-1	125	ol gb	med	9	0.6	shd	prm, elg	rrm	54	0.2	shd	prm, elg	cc	37	0.3	shd	prm	oc
OM10-Sam_5-2	127.5	ol gb	med	11	0.7	shd	prm	rrm	56	0.3	shd	prm, elg	cc	33	0.5	shd	prm, irg	oc
OM10-Sam_5-3	131.9	ol gb	med	23	1.0	shd	prm	oc, rrm	49	0.3	shd	prm, elg	cc	28	0.4	shd	prm	oc
OM10-Sam_4-1	173	ol-b gb	fin	2	2.0	shd	prm, elg	oc, rrm	57	0.8	shd	prm, elg	cc	41	0.6	shd	prm	oc
OM10-Sam_4-2	176.5	ol-b gb	med	2	2.0	shd	prm, elg	oc, rrm	58	0.5	shd	prm, elg	cc	40	0.7	shd	prm	oc
OM10-Sam_4-3	180	ol-b gb	fin	1	1.0	shd	prm, elg	oc, rrm	62	0.4	shd	prm, elg	cc	37	0.5	shd	prm	oc
OM10-Sam_4-4	183	ol-b gb	med	2	1.5	shd	prm, elg	oc, rrm	68	0.5	shd	prm, elg	cc	30	0.5	shd	prm	oc
OM10-Sam_3-1	198	ol gb	med	12	2.0	shd	prm, irg	oc, rrm	29	0.5	shd	prm, elg	cc	59	2.0	shd	prm	oc
OM10-Sam_3-2	200	ol gb	med	13	2.0	shd	prm, irg	oc, rrm	24	0.5	shd	prm, elg	cc	63	2.5	shd	prm	oc
OM10-Sam_3-3a	202	ol gb	med	10	1.5	shd	prm, irg	oc, rrm,	34	0.5	shd	prm, elg	cc	56	2.0	shd	prm	oc
OM10-Sam_3-3b	207	ol-b gb	med	1	1.8	shd to ehd	prm	oc, rrm	56	0.4	shd	prm, elg	cc	43	1.5	shd	prm	oc
OM10-Sam_2-1	220	ol-b gb	fin	4	2.0	shd	prm, elg	oc, rrm	62	0.3	shd	prm, elg	cc	34	1.0	shd	prm	oc
OM10-Sam_2-2	222.1	ol-b gb	fin	9	1.5	shd	prm	oc, rrm,	62	0.3	shd	prm, elg	cc	29	0.8	shd	prm	oc
OM10-Sam_2-3	225.1	ol-b gb	fin	5	1.5	shd	prm	oc, rrm	71	0.3	shd	prm, elg	cc	24	0.7	shd	prm	oc
OM10-Sam_1-1	267.9	ol gb	med	17	2.0	shd	prm, irg	oc, rrm	34	0.4	shd	prm, elg	cc	49	2.0	shd	prm	oc
OM10-Sam_1-2	271.2	ol gb	med	14	1.8	shd	prm, irg, elg	oc, rrm	61	0.3	shd	prm, elg	cc	25	1.8	shd	prm	oc

Table 1
Continued

Sample	DiS (cm)[a]	Lithology[b]	Grain size mode[c]	Olivine					Plagioclase					Clinopyroxene				
				Mode (%)[d]	GS (mm)[e]	Shape[f]	Habit[g]	Comment[h]	Mode (%)[d]	GS (mm)[e]	Shape[f]	Habit[g]	Comment[h]	Mode (%)[d]	GS (mm)[e]	Shape[f]	Habit[g]	Comment[h]
OM10_War_DS1-11	0.5	ol gb	med	15	1.5	shd	prm, elg	oc	65	0.4	shd	prm, elg	cc	20	1.5	shd	prm	rare oc
OM10_War_DS1-10	1.2	ol gb	med	15	1.5	shd	prm, irg	oc	55	0.7	shd	prm, elg	cc	30	1.5	shd	prm	
OM10_War_DS1-9	1.9	ol gb	med	12	1.5	shd	prm, irg	oc	58	0.5	shd	prm, elg	cc	30	1.2	shd	prm	
OM10_War_DS1-8	2.5	ol gb	med	18	1.0	shd	prm, irg	oc	62	0.5	shd	prm, elg	cc	20	1.0	shd	prm	rare oc
OM10_War_DS1-7	3.1	ol gb	med	10	1.0	shd	prm, irg	oc	60	0.6	shd	prm, elg	cc	30	0.8	shd	prm	
OM10_War_DS2-6	3.8	ol gb	med	16	1.2	shd	prm, irg		57	0.6	shd	prm, elg		27	0.7	shd	prm	
OM10_War_DS2-5	4.1	ol gb	med	18	1.2	shd	prm, irg		55	0.5	shd	prm, elg		27	0.5	shd	prm	
OM10_War_DS2-4	4.8	ol gb	med	15	1.3	shd	prm, irg		50	0.5	shd	prm, elg		35	0.6	shd	prm	
OM10_War_DS2-3	5.6	ol gb	med	20	1.3	shd	prm, irg		50	0.5	shd	prm, elg		30	0.6	shd	prm	
OM10_War_DS2-2	6.2	ol gb	med	7	1.0	shd	prm, irg		62	0.5	shd	prm, elg		30	0.6	shd	prm	
OM10_War_DS2-1	7	ol-b gb	fin	3	1.5	shd	irg, elg	skl	55	0.4	shd	prm, elg	cc	42	0.5	shd	prm	

Note. Horizontal lines mark layer boundaries; dashed horizontal lines mark the transition from leucocratic layer top to melanocratic layer base. [a]Depth of the sample within the sequence. [b]Gb = gabbro, ol-b gb = olivine-bearing gabbro (<5% olivine), ol gb = olivine gabbro (>5% olivine). [c]Grain size range of the entire thin-section domain with med = medium grained (>1–5 mm) and fin = fine grained (>0.2–1 mm). [d]Modal proportions per phase in area % by visual estimation. [e]Diameter or long-axis length for elongated grains averaged by the long axis measurements of ten grains per sample. [f]Grain shape with shd = subhedral, ehd = euhedral. [g]Grain habit with prm = prismatic, elg = elongated, irg = irregular. [h]Observed special features with oc = oikocrysts, rrm = reaction rim, skl = skeletal, cc = chadacrysts.

Table 2
Trace Element Compositions in Clinopyroxene and Plagioclase Given in ppm and Crystallization Temperature Estimated After Sun and Liang (2017) for Wadi Somerah

#[a]	Type[b]	Sample	Depth (cm)[c]	Phase[d]	Loc[e]	n[f]	Intem std (wt%)[g]	Zr	La	Ce	Pr	Nd	Sm	Eu	Gd	Tb	Dy	Y	Ho	Er	Tm	Yb	Lu	T_{REE} (°C)[h]	±1σ[i]
6	m	OM10-Sam_11	4	pl	co	16	16.87	0.02	0.477	1.073	0.145	0.597	0.114	0.351	0.095	0.012	0.055	0.256	0.009	0.019	0.002	0.009	0.001	1,270	13
				cpx	co	16	21.71	4.99	0.125	0.705	0.185	1.287	0.709	0.277	1.143	0.226	1.515	8.475	0.319	0.898	0.126	0.799	0.115		
					ri	14	21.56	8.39	0.164	0.860	0.229	1.654	0.923	0.304	1.490	0.294	1.963	11.577	0.431	1.235	0.176	1.087	0.167		
5	m	OM10-Sam_9-1	49.9	pl	co	19	16.94	0.02	0.248	0.531	0.080	0.358	0.074	0.232	0.068	0.008	0.038	0.189	0.006	0.014	0.002	0.008	0.001	1,232	10
				cpx	co	14	21.76	7.16	0.169	0.808	0.219	1.642	0.904	0.350	1.551	0.302	2.068	11.647	0.435	1.206	0.175	1.060	0.157		
					ri	15	21.68	9.18	0.172	0.816	0.230	1.798	1.001	0.368	1.762	0.345	2.359	13.715	0.504	1.378	0.206	1.204	0.184		
4	l	OM10-Sam_6-2	108.7	pl	co	24	16.77	0.01	0.280	0.640	0.089	0.397	0.084	0.277	0.069	0.008	0.039	0.188	0.007	0.014	0.002	0.008	0.001	1,264	17
				cpx	co	16	21.79	4.51	0.112	0.617	0.159	1.160	0.634	0.258	1.038	0.203	1.352	7.633	0.289	0.812	0.115	0.692	0.101		
					r	15	21.59	7.32	0.134	0.693	0.184	1.395	0.806	0.276	1.319	0.264	1.754	10.257	0.381	1.079	0.151	0.927	0.140		
3	m	OM10-Sam_5-2	127.5	pl	co	17	17.24	0.02	0.203	0.500	0.064	0.279	0.056	0.204	0.046	0.005	0.024	0.109	0.004	0.009	0.001	0.005	0.000	1,230	12
				cpx	co	30	22.13	5.79	0.153	0.849	0.212	1.550	0.848	0.321	1.329	0.249	1.755	9.163	0.360	0.995	0.138	0.906	0.129		
					r	20	22.48	8.53	0.160	0.870	0.233	1.788	0.951	0.331	1.656	0.317	2.229	12.118	0.473	1.308	0.177	1.145	0.163		
3	l	OM10-Sam_4-4	153.9	pl	co	28	16.86	0.02	0.181	0.425	0.064	0.296	0.070	0.219	0.066	0.009	0.047	0.229	0.008	0.018	0.002	0.011	0.001	1,233	6
				cpx	co	15	21.83	6.58	0.154	0.774	0.215	1.598	0.869	0.342	1.483	0.290	1.938	10.747	0.399	1.126	0.162	0.967	0.141		
					ri	12	21.77	12.80	0.181	0.950	0.273	2.044	1.173	0.376	2.114	0.416	2.776	16.140	0.590	1.666	0.236	1.425	0.216		
2	m	OM10-Sam_3-3a	202.7	pl	co	21	16.86	0.01	0.339	0.770	0.102	0.426	0.086	0.278	0.067	0.008	0.038	0.176	0.006	0.013	0.001	0.006	0.001	1,273	14
				cpx	co	18	21.94	6.69	0.165	0.817	0.215	1.575	0.860	0.335	1.412	0.266	1.847	10.227	0.398	1.082	0.151	0.916	0.135		
					ri	43	22.05	8.54	0.213	0.954	0.256	1.850	1.002	0.361	1.741	0.325	2.309	13.276	0.490	1.399	0.199	1.184	0.176		
1	l	OM10-Sam_3-3b	204.7	pl	co	21	16.95	0.01	0.235	0.582	0.081	0.354	0.072	0.237	0.061	0.007	0.033	0.162	0.006	0.012	0.001	0.006	0.001	1,233	12
				cpx	co	29	22.00	5.65	0.151	0.816	0.204	1.531	0.809	0.335	1.314	0.249	1.707	9.052	0.360	0.997	0.134	0.872	0.121		
					ri	24	21.85	7.26	0.161	0.883	0.221	1.697	0.911	0.352	1.477	0.278	1.912	10.508	0.410	1.140	0.156	0.990	0.139		
1	m	OM10-Sam_1-1	267.9	pl	co	13	17.05	0.04	0.538	1.079	0.142	0.640	0.135	0.406	0.117	0.013	0.069	0.309	0.012	0.023	0.003	0.012	0.001	1,297	18
				cpx	co	15	21.87	6.45	0.132	0.639	0.169	1.336	0.742	0.274	1.233	0.241	1.601	9.360	0.349	0.972	0.139	0.842	0.125		
					ri	14	21.45	15.67	0.205	0.979	0.264	2.061	1.079	0.320	1.821	0.357	2.375	14.444	0.517	1.484	0.217	1.316	0.202		

[a]Layer number corresponding to the numbers given in Figure 2b. [b]Layer specifier with m = melanocratic for dark, ol-rich layer bases, and l = leucocratic for bright, ol-poor layer tops. [c]Depth of the sample within the sequence. [d]Represents pl = plagioclase, cpx = clinopyroxene. [e]Location of analysis with co = core and ri = rim. [f]Number of measurements that is averaged. [g]CaO concentration in wt% for internal standardization. [h]Crystallization temperature calculated after Sun and Liang (2017). [i]Standard error of the regression line provided by the Sun and Liang (2017) excel sheet.
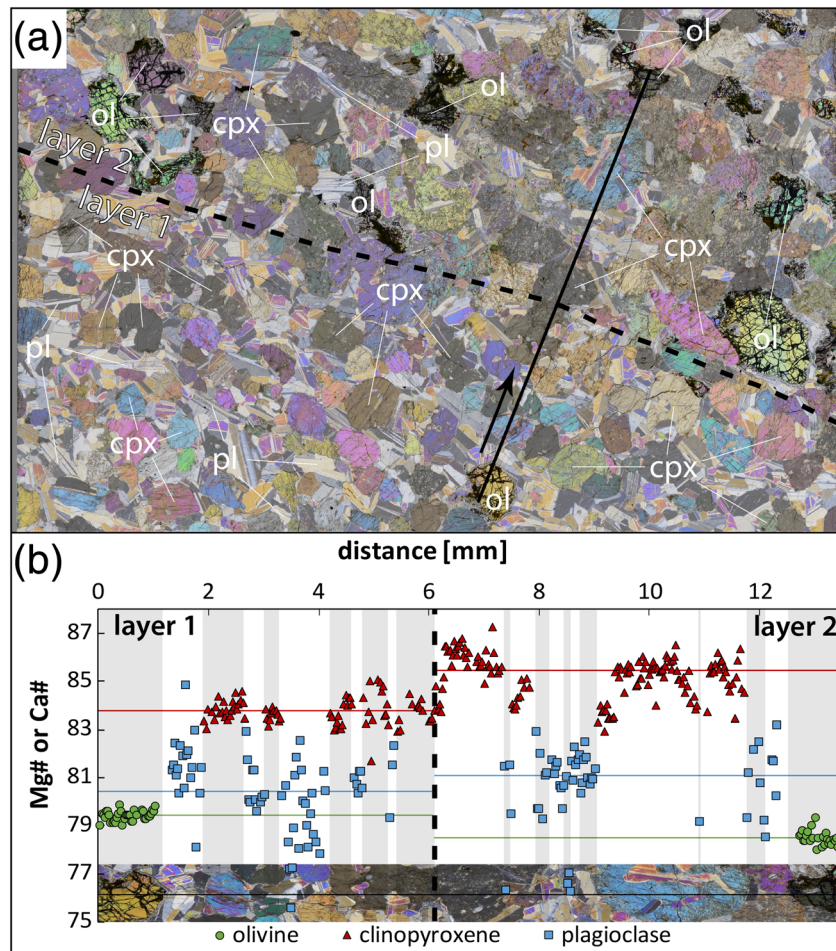
Figure 5. (a) Cross-polarized thin-section photograph of the layer boundary between layers 1 and 2 from Wadi Somerah; ol = olivine, cpx = clinopyroxene, pl = plagioclase. Black line gives the position of the EPMA profile; the black arrow marks its direction. Dashed black line marks the layer boundary deviated from modal proportions. Note the significantly increased olivine content at layer 2. Image width = 2 cm. (b) Mg#s of clinopyroxene and olivine and Ca# of plagioclase plotted along the profile given in (a). Green circles give olivine, red triangles clinopyroxene, and blue rectangles plagioclase data. The image at the bottom shows the profile position, cropped and rotated from (a). The gray and white bars symbolize individual grains. Horizontal colored lines give median for layer 1 or layer 2, respectively, with green = Mg# in ol, red = Mg# in cpx, and blue = Ca# in pl. Note its changes at 6 mm coinciding with the layer boundary in (a).

deviation of 24°C. Considering the data and model uncertainties, which lead to uncertainties of about 50°C, we assess the crystallization temperatures as being more or less constant along the profile.

The cooling rates obtained by Ca-in-olivine calculations using the thermometer of Shejwalkar and Coogan (2013) result in slow cooling rates between 1.2°C/kyr and 22°C/kyr with an average of 7°C/kyr ($\log[dT/dt] = -2.21°C \pm 0.7°C \, \text{yr}^{-1}$) and closure temperatures of 910°C to 965°C in the core. Using Mg-in-plagioclase after Faak et al. (2014) for an estimate of the cooling rate does not provide reliable results for Wadi Somerah samples due to Mg contents in plagioclase falling below the detection limit of about 0.005 wt%. The very low closure temperature of 550°C modeled for a putative MgO content of 0.005 wt% is far below the closure temperatures calculated using Ca-in-olivine and indicates much slower cooling. Before the background of the misfit between the two applied methods, and taking indicators for hydrothermal alteration of the sampled material into account, we interpret the low MgO contents in plagioclase from Wadi Somerah as result of secondary reactions (e.g., dissolution-reprecipitation) rather than solid-state diffusion as it was already observed in samples in recent lower oceanic crust by Faak et al. (2015).
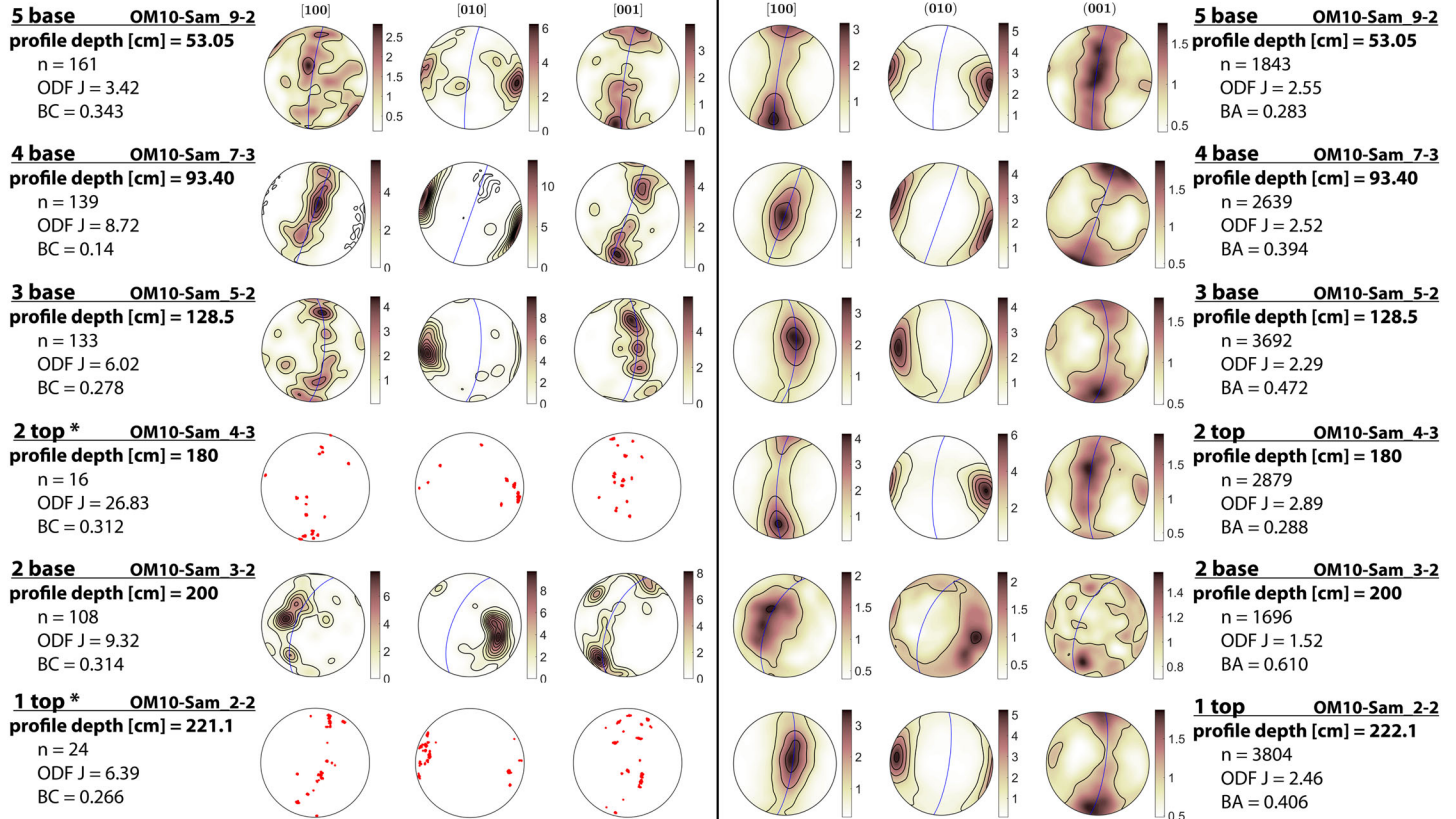
Figure 6. Representative pole figures for crystallographic axes [100], [010], and [001] of olivine (a) and the crystallographic axes or poles [100], (010), and (001) of plagioclase (b) in Wadi Somerah. The pole figures are arranged by their height in the sequence; text block aside gives the layer number and the sample position within the layer (base/top), the depth in the layered sequence, the corresponding BA or BC index, and the ODF J index of the sample. *N* is the number of analyzed grains. The blue line gives the foliation estimated from (010) of plagioclase. The star behind a layer number indicates a low number of analyzed grains (<70). Patterns with a point of every analyzed pixel are plotted for samples with <70 analyzed grains because contoured pole figures are not significant here. Note the differently scaled color bars.

The orientation of our samples was not documented during collection. Therefore, the pole figures and indicated orientations of fabric features can only be interpreted on the thin-section scale and not at outcrop or crustal scales. Nonetheless, the pole figures of olivine and plagioclase obtained by EBSD reveal remarkable observations (see Figure 6; all pole figures are compiled in Mock et al., 2020a). Except for the base of layer 2, which is described in more detail below, the pole figures show relatively similar features. Plagioclase shows distinct maxima in (010) coupled with weak maxima of [100]. Maxima in plagioclase [100] are most dominant at layer 5 top, layer 4 base, and layer 3, therefore indicating a slightly more linear fabric in these layers. Most olivine fabrics of this section also shows well-pronounced [010] maxima and more modest [001] maxima. Olivine [100] maxima at layer 4 base, layer 2 top, and layer 1 top correlating with plagioclase [100] lineation possibly indicate some plastic deformation overprint (although layer 2 top and layer 1 top should be read with caution due to the low number of measured olivine grains). At the bases of layer 5 and layer 3, olivine [001] correlates with plagioclase [100], suggesting a weak (010) [001] olivine fabric, which can be ascribed to magmatic flow (e.g., Jousselin et al., 2012). In contrast to these more or less well-pronounced fabrics, the layer 2 base has at most only a very weak plagioclase fabric. The number of analyzed olivine grains is very low here, such that the results cannot be as representative as those of plagioclase; the pole figures show maxima in all crystallographic axes.

The nearly absent fabric at the base of layer 2 is reflected by a low plagioclase ODF J index of 1.52 (Figures 4 and 6). Importantly, the minimum ODF J here correlates with the minimum in olivine Mg# and plagioclase

Ca#. Furthermore, the corresponding samples are the only ones in the entire profile where the modal abundance of clinopyroxene is significantly higher than that of plagioclase and clinopyroxene grain sizes are clearly higher when compared with the surrounding tops of layers 1 and 2. Very low internal misorientations in plagioclase and clinopyroxene (GOS < 0.5° in both phases) imply that samples from Wadi Somerah did not experience significant intracrystalline deformation.
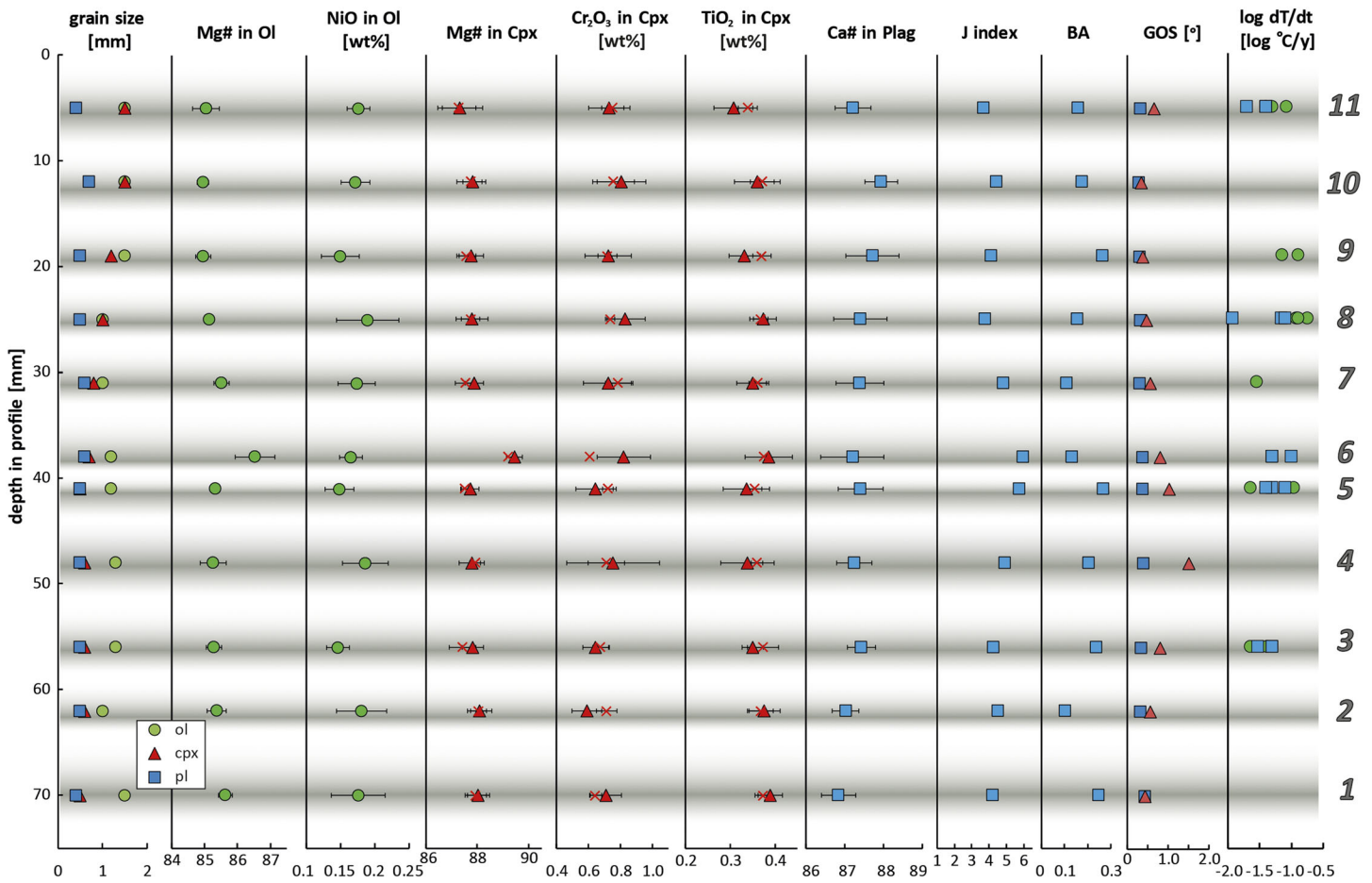
4.2. Wadi Wariyah

Due to the millimeter-scale layering in the sample from Wadi Wariyah, it is not possible to clearly assign crystals to either the melanocratic base of a layer or its leucocratic top. Thus, only average values are given for individual layers. The millimeter-scale layers from Wadi Wariyah contain between 3% (layer 1) and 20% (layer 3) olivine, 50% (layer 3 and 4) to 65% (layer 11) plagioclase, and 20% (layers 8 and 11) to 40% (layer 1) clinopyroxene (see Table 1 for modal proportions of every layer). Olivine is enriched in diffuse, millimeter-scaled bands defining the observed layering. All layers in the sample from Wadi Wariyah are classified as olivine gabbro (>5 modal % olivine) except for layer 1 which is classified as olivine-bearing gabbro. The EBSD phase map in Figure 3c shows the sample OM10-War_DS1 which covers the upper five millimeter layers from Wadi Wariyah. Note the fine differences in olivine abundance from base to top of every layer. Plagioclase shows a homogeneous, sub-millimeter, crystal long-axis length along the sequence whereas olivine grains are larger (1–1.5 mm on average). Clinopyroxene shows the largest grains in layer 1 with a 1.5-mm average size, but the grain size gradually decreases down section to a minimum of 0.5 in layer 5. Clinopyroxene size is then constant from layer 1 to layer 5. As for the Wadi Somerah samples, grain shape is commonly subhedral, olivine is irregular, whereas plagioclase occasionally forms elongated laths. Poikilitic or skeletal olivine and clinopyroxene crystals containing plagioclase indicate a similar crystallization sequence to that inferred from Wadi Somerah. The petrographic results from Wadi Wariyah are summarized in Table 1.

The microprobe data from Wadi Wariyah (see collected data in Mock et al., 2020a) reveal Mg# values of olivine and clinopyroxene ranging between 85.0 and 86.5, and 86.3 and 89.0, respectively (Figure 7). The Mg# of olivine slightly decreases up section with a significantly outlier at layer 6. The NiO content ranges between 0.1 and 0.2 wt%. The Mg# of clinopyroxene shows an evolution similar to that of the Mg# in olivine with nearly constant values along the sequence and with a distinct maximum of 89.0 at layer 6. The evolution of Cr_2O_3 is correlated with that of the Mg#. We observe clear trends in the TiO_2 content in clinopyroxene, which is positively correlated with Mg# in layer 6. Both Cr_2O_3 and TiO_2 show significant differences in core and rim compositions which do not, however, represent systematic zonation. The Ca# varies within a small range between 86.7 and 87.9, thus generally higher than in Wadi Somerah, with a slight increase up section from layer 2 to 11 and a marked decrease to layer 1. However, the Ca# does not show its maximum in layer 6, as may be expected from elevated Mg# in olivine and clinopyroxene, here.

Cooling rates in Wadi Wariyah were estimated using both Ca-in-olivine and Mg-in-plagioclase speedometers. Both methods reveal broadly similar cooling rates within a wide range of 12 to 180°C/kyr, with an average of 81°C/kyr ($\log[\mathrm{d}T/\mathrm{d}t] = -1.19 \pm 0.5$°C yr^{-1} using Ca in olivine) and 51°C/kyr ($\log[\mathrm{d}T/\mathrm{d}t] = -1.35$°C ± 0.6°C yr^{-1} using Mg in plagioclase) (see Mock et al., 2020a). Compared to Wadi Somerah, subsolidus cooling in Wadi Wariyah was up to one and a half orders of magnitude faster. The closure temperatures calculated for plagioclase rims vary from 850 to 930°C.

The pole figures obtained for every layer of the Wadi Wariyah profile are very similar (Figure 8; see compiled pole figures for Wadi Wariyah Mock et al. (2020a)) with a consistent distinct maximum of plagioclase (010) and well-pronounced girdle with weak point maxima of [100]. This dominantly planar plagioclase fabric is reflected by olivine with maxima of [010] and girdles with weak point maxima of both [100] and [001] of every layer, therefore suggesting a compaction-dominated regime. Magmatic lineation, as we found indicated by olivine fabrics in Wadi Somerah, are less distinct in Wadi Wariyah, and only suggested by the correlating weak point maxima in [100] and [001] in plagioclase and olivine, respectively. These findings are well-represented by low values for the BA and the BC indices in plagioclase and olivine, respectively, of up to 0.28. Only the BC of olivine, being calculated from a relatively small number of grains, reaches 0.6 in layer 6. The ODF J index of 3.71 to 6.01 for plagioclase is slightly higher than the one from Wadi Somerah. Calculating the ODF J index for only 300 randomly chosen plagioclase grains of every sample from both locations confirmed that the increased ODF J index in Wadi Wariyah is not a mathematical artifact

Figure 7. Summarized results of analyses on the millimeter-scale layered gabbro sequence from Wadi Wariyah. Gray numbers on the right give the layer number; gradational gray background symbolizes the layer color, most pronounced by olivine content. Closed symbols are core; crosses are rim analyses. Black bars give 1 sigma standard deviation from the mean. Mg# = Mg/(Mg + Fe) × 100; molar basis, Ca# = Ca/(Ca + Na) × 100; molar basis. GOS = grain orientation spread. See text for further interpretation.
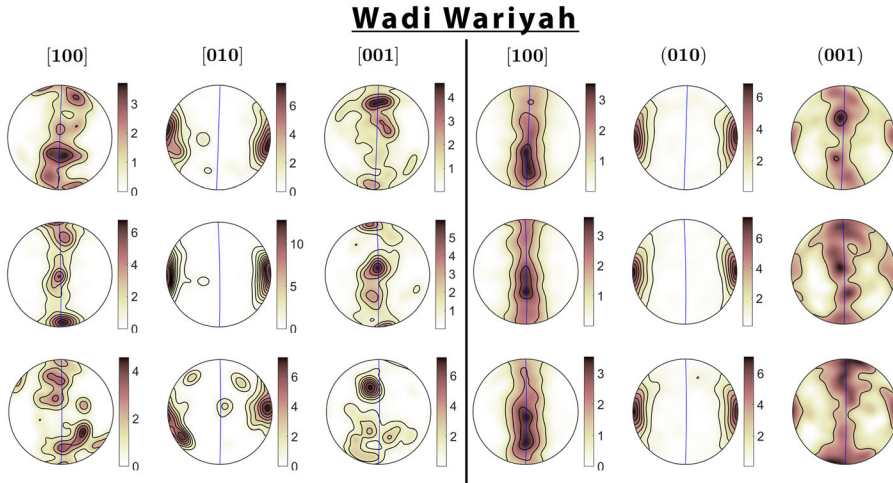
Figure 8. Representative pole figures for crystallographic axes [100], [010] and [001] of olivine (a) and axes or poles [100], (010) and (001) of plagioclase (b) in Wadi Wariyah. The pole figures are arranged by their height in the sequence; text block aside gives the layer number, the depth in the layered sequence, the corresponding BA or BC index, and the ODF J index of the sample. *N* is the number of analyzed grains. The blue line gives the foliation estimated from (010) of plagioclase. Note the differently scaled color bars.
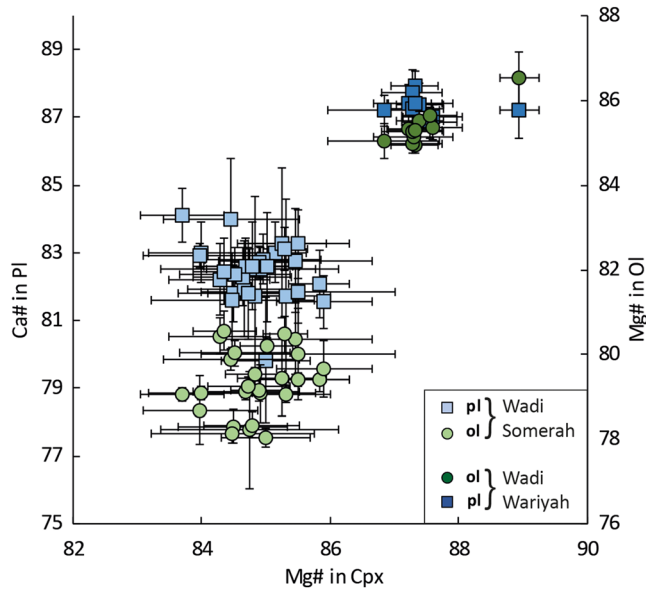
Figure 9. Ca# ((Ca/Ca + Na) × 100; molar basis) in plagioclase and Mg# ((Mg/Mg#Fe) × 100; molar basis) in olivine plotted versus Mg# in clinopyroxene. Blue rectangles are plagioclase data, green circles are olivine data. Lighter colors belong to samples from Wadi Somerah, darker to Wadi Wariyah. Error bars symbolize one sigma standard deviation from the mean.

resulting from analyzing a smaller number of analyzed grains. Misorientation is low—similar to Wadi Somerah—with only clinopyroxene revealing slightly elevated values (GOS < 1.5°). Nevertheless, the low values also suggest weak or no impact of intracrystalline deformation in Wadi Wariyah.

5. Discussion

5.1. Our Data in the Context of Previous Studies

Data from this study can be interpreted in the context of many previous works on Oman. The layering of the oceanic crust as observed in Wadi Somerah is well-known from Oman gabbros and has already been described by many authors (e.g., Browning, 1984; Pallister & Hopson, 1981). These authors observed large-scale correlating variations in major and minor element distributions of the three near-liquidus phases olivine, plagioclase, and clinopyroxene in the crust. In contrast to these studies, our spacing is very fine with a maximum of 42 cm between two thin sections. As Pallister and Hopson (1981) and Browning (1984) already noted, we see general inter-phase correlations in terms of major element composition at the base of layer 2 in our profile from Wadi Somerah where Mg# in olivine, Ca# in plagioclase, and Mg# in clinopyroxene rims follow the same fractionation trend. A simple explanation for this behavior could be an increased amount of trapped melt within this region. A longer time to equilibrate the minerals with the trapped melt leads to more fractionated melt- and therefore evolved mineral compositions. This scenario is consistent with fast Mg/Fe diffusion in olivine (Chakraborty, 1997) equilibrating initial core-rim zonation which is hence no longer observed in our samples. In clinopyroxene, a core-rim zonation can still be observed due to slower Mg/Fe interdiffusion (e.g., Dimanov & Sautter, 2000). Simultaneous Ti enrichment in the rim is consistent with Ti diffusion being 1–3 orders of magnitude slower in pyroxenes than the diffusion of Mg and Fe (Cherniak & Liang, 2012). However, the coupled Na + Si/Ca + Al diffusion in plagioclase is very slow (e.g., Morse, 1984) implying that the observed lack of zoning is primary and plagioclase crystallization did not occur within a trapped liquid. Apart from at the base of layer 2 base, our data do not show significant trends, and no further inter-phase correlations are observed, in part due to analytical uncertainties being large with respect to the very limited compositional variation present at Wadi Somerah (Figure 9). It can be argued that inter-phase correlations are overprinted by post-cumulus percolation of evolved melt interacting with the cumulates (e.g., Jansen et al., 2018; Lissenberg et al., 2013), but indicators for such processes, for example, strong enrichment of trace elements from core to rims in clinopyroxene, are only weakly developed in our samples. We found a maximum enrichment of Zr in the rim by a factor of 2.4 compared to its core in a single sample. Other trace elements show weaker rim/core enrichments, with observed factors reaching a maximum of 1.6. Also, the rim/core ratios of Zr/Nd and Ce/Y give relatively homogeneous element distributions with values up to 1.6 and down to 0.8, respectively. In contrast, rim/core enrichment factors of up to 15 were reported for deep gabbros from Hess Deep where melt percolation is assumed to have taken place (Lissenberg et al., 2013). However, interpreting these data needs consideration of diffusivity of these elements which tends to balance differences and therefore could weaken the initial degree of zonation. As Sun and Liang (2017) point out, diffusion of REEs in clinopyroxene and plagioclase is significantly slower than Mg diffusion in both minerals. This first explains why REE zonation in clinopyroxene is more systematic than the zonation of Mg (Figure 10) and second indicates that initial zonation was not much stronger than the zonation we observed in our samples. Taking the cooling rate of up to 22°C/kyr into account which limits the efficient equilibration of REEs due to their low diffusivities (e.g., Sun & Liang, 2017), enrichment factors of ~15 as found by Lissenberg et al. (2013) at Hess Deep are absent in our profile from Wadi Somerah. Therefore, we assume that the influence of percolating porous melt was very limited in our samples.

Values of differentiation indices in Wadi Wariyah close to the MTZ are lower than typical numbers from mantle olivines in Oman (Fo > 90; e.g., Tamura & Arai, 2006), indicating that the melt has undergone
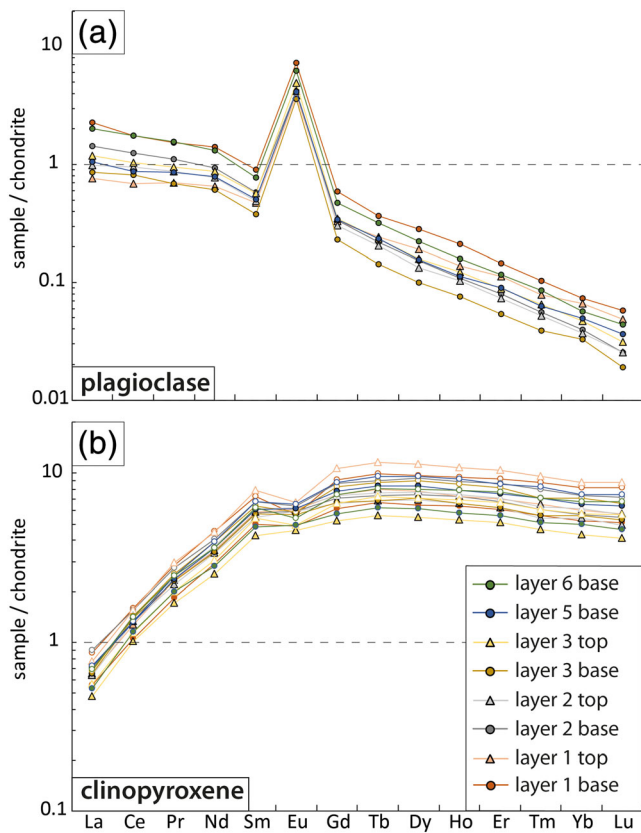
Figure 10. Chondrite-normalized rare earth element data in (a) plagioclase and (b) clinopyroxene. Chondrite values from McDonough and Sun (1995). Circles symbolize data from layer bases and tringles from the tops. Closed symbols are core; open symbols are rim data.

some crystallization since leaving the mantle. Defining the crustal region where differentiation of the melt occurred is, however, beyond the scope of this study. Our data are in good agreement with most of the fractionation indices obtained by Korenaga and Kelemen (1997) who sampled modally layered gabbros from the MTZ. However, in contrast with our results, they also found that phase compositions correlated with modal proportions. Since these variations occur on a millimeter to centimeter scale, they conclude that the modal layering they observed cannot have formed by crystal settling as this would have led to relatively high porosities eliminating fine chemical variations by equilibration with interstitial melt.

### 5.2. The Formation of Igneous Layering in Profiles From Wadi Somerah and Wadi Wariyah

Layer-forming processes have been reviewed in detail by Naslund and McBirney (1996) and more recently Namur et al. (2015) who also argued that they can generally be separated into dynamic (i.e., occur during filling or crystallization of a magma chamber) and non-dynamic (i.e., rapid changes in intensive conditions of crystallization) layer-forming processes and that they range from physical processes (e.g., gravitational sorting) to tectonic (e.g., seismic shocks) and chemical ones (e.g., dissolution-precipitation). Many of these processes can occur in any given magmatic system, and none of them are thought to be exclusively responsible for any distinct type of layering. We provide a compilation and brief evaluation of 31 layer-forming processes (according to Namur et al., 2015) that are potentially relevant to our samples in the electronic supplement, and we discuss the processes which find at least partial support in our data in detail below. Providing a full overview of all layer-forming processes is, however, beyond the scope of this work.

5.2.1. Magma Injection

Correlated changes in major mineral compositions and crystallographic preferred orientations (Figure 4) in layer 2 from Wadi Somerah indicate that the formation of this particular section of the profile was accompanied by processes affecting the mechanical and chemical properties of the rock. One explanation considered above invokes an increased amount of trapped melt at the base of layer 2 leading to more fractionated minerals. An alternative explanation for a compositional shift toward more primitive phase compositions at the top of layer 2 could be the influx of more primitive melt, provoked by a replenishment process. We see evidence for such an event in the different phase compositions between the base and the top of layer 2: while the compositions follow a clear fractionating trend from layer 1 top to the base of layer 2, with decreasing Mg# correlating with decreasing NiO in olivine, decreasing Ca# correlating with increasing Ce in plagioclase, and decreasing Mg# correlating with increasing TiO_2 and Cr_2O_3 contents at the rim of clinopyroxene, the compositions at the top of layer 2 show more primitive signals. The Mg# of olivine is increased compared to the base of layer 2, the Ca# of plagioclase as well which correlates with a decreased Ce content. Also, the rim values of TiO_2 and Cr_2O_3 in clinopyroxene decreased from the base of layer 2 toward its top, indicating that the top of layer 2 crystallized from a more primitive melt than the base of this layer.

A remarkable change in rock fabric occurring between the base and the top of layer 2 (i.e., no fabric at the base, plagioclase (010) maximum with [100] girdle, copied by [010] and [001] of small amounts of analyzed olivine; Figure 6a, see pole figure compilation in Mock et al., 2020a) coincides with the shifts in mineral compositions described above. Although an increased amount of trapped melt at the base of layer 2 can explain most of the observed variation in phase compositions, the absence of a clear rock fabric appears more consistent with the hypothesis that the base of layer 2 crystallized in a system with only limited amounts of melt where solid phase mobility was reduced. However, the magmatic fabric at the top of the same layer indicates a higher liquid/solid ratio, which would in turn result in higher crystal mobility enabling crystals to orient
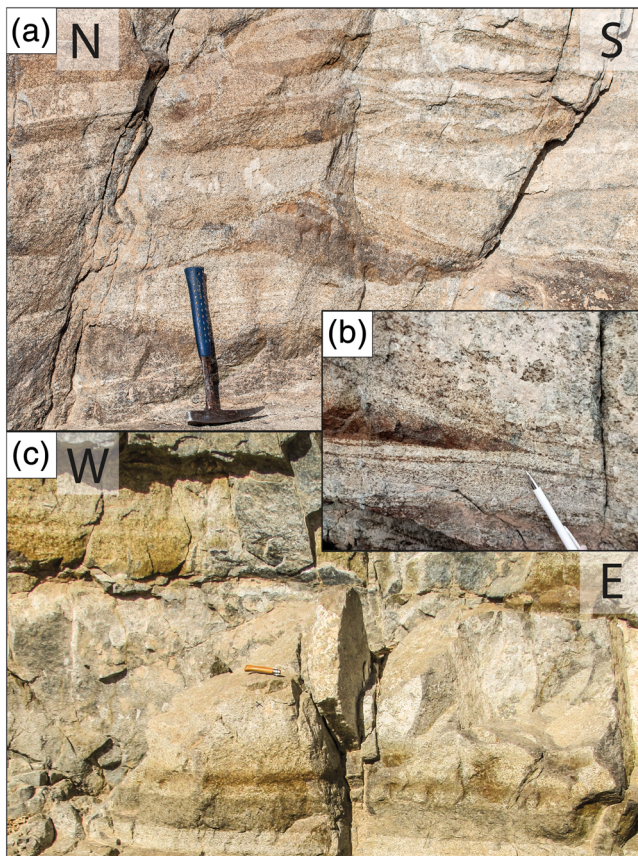
Figure 11. (a) Centimeter- to decimeter-scaled disturbed modal layering at the western flank of the Wadi Somerah outcrop. (b) Centimeter-scaled layer cross cutting a layer deposited before at the southern front of the outcrop in Wadi Somerah. (c) Decimeter-scaled laminar horizontal modal layering at the southern front of the Wadi Somerah outcrop. Knife as scale bar with a length of about 10 cm. Orientation directions given in black in (a) and (c). Note the significant difference in the appearance between (a) and (b), and (c). Photographs by D. Mock and P. E. Wolff.

and form the observed foliation. We therefore argue that the shift toward more primitive phase compositions at the top of layer 2 could also be interpreted as indicators for a magma replenishment affecting both chemical and textural features of the sample. If this interpretation is correct, we infer that localized melt injections are possible within the lower crust.

If magma replenishment occurs within the lower oceanic crust, is it able to trigger modal layering formation by resetting the crystallization sequence? Correlating every layer with an individual pulse of fresh magma would create correlations between phase compositions and the layer height and therefore, in case of modal layering, also between phase compositions and mineral abundances. This was observed by Korenaga and Kelemen (1997) who found that olivine-rich sections were more primitive in terms of Fo in olivine and partially also Cr in clinopyroxene. They concluded that the melt lens composition could be reset by expulsion of melt through hydrofractures and repetitious expulsion and replenishment could create modal layering. While this interpretation is relevant to their data, it is inconsistent with the absence of layer-correlated compositional trends from our profiles. Although magma replenishment can cause chemical and textural variability within the lower crust, it does not seem to have driven the formation of modal layering in the samples we have studied.

5.2.2. Gravitational Sorting by Crystal Settling

The concentration of the denser phases—olivine and clinopyroxene—and the deficit of plagioclase at the base of each layer lead to the intuitive suggestion that gravitational sorting plays a key role in the formation of the modal layering in the Wadi Somerah sequence. Theoretically, an increased water activity expected for Oman paleo-magmatism (e.g., MacLeod et al., 2013; Müller et al., 2017; Pearce et al., 1981) could restrict plagioclase nucleation and therefore result in layers being depleted in plagioclase (or even wehrlitic layers which we do not observe in our profiles; e.g., Feig et al., 2006). However, the water content of 0.4–0.8 wt% estimated for the melt beneath the Oman spreading center by Müller et al. (2017) is insufficient to fully suppress plagioclase nucleation in basaltic melts (Feig et al., 2006; Gaetani et al., 1993). Furthermore, poikilitic olivine and clinopyroxene hosting plagioclase chadacrysts makes it clear that plagioclase crystallization occurred—at least in part—simultaneously with olivine and clinopyroxene.

Korenaga and Kelemen (1997) conclude that crystal settling could not have formed modal layering in the Maqsad area since the large porosity in a cumulate formed by crystal settling was inconsistent with the millimeter-scale modal variation they observed in their samples. However, such systematic small-scale correlations between modal proportions and phase compositions have not been observed in our samples. Nonetheless, if a magmatic system contains enough melt to mobilize solid particles, density-controlled phase segregation and therefore modal layering may be formed. However, if density-controlled phase segregation occurs, a process is required to explain the rhythmic layer sequence that we observe. Possibly, every layer could represent a completely crystallized individual sill (cf., the sheeted sills model; e.g., Kelemen et al., 1997). However, the crystallization from individual sills would be expected to result in greater chemical differences between the layers, demanding a physical barrier between layers of sill intrusion into already solidified hence colder surrounding gabbro. The limited variation in our petrological and chemical data does not agree with every layer having formed from a different sill. Sparks et al. (1993) instead suggested that intermittent convection could form cyclic layering in a magma chamber: At a high convection velocity, crystals can be kept in suspension and will settle down as soon as the convection velocity decreases or stops. Following Stoke's law, denser crystals will settle faster and are therefore accumulated at the base of the convective subunit. Repeated changes in convection velocity would lead to rhythmic deposition of several layers.

In order to evaluate the potential role of gravitational sorting on layer formation, we modeled the settling velocities of olivine, plagioclase, and clinopyroxene. As parental melt composition, we considered the average Samail melt composition estimated by Pallister and Gregory (1983) with water contents between 0.4 and 0.8 wt% (MacLeod et al., 2013; Müller et al., 2017). We used the models of Giordano et al. (2008) and of Ueki and Iwamori (2016) to estimate the viscosity and the density of the melt, respectively, at a pressure of 0.2 GPa and in a temperature range of 1230°C–1300°C, according to the calculated crystallization temperatures given by the Sun and Liang (2017) REE thermometer. The resulting liquid parameters were applied to the Stoke's law equation, taking into account the densities of olivine, plagioclase, and clinopyroxene as well as their estimated grain sizes. The results show that plagioclase would float (or "rise" with a velocity in the range of 10^{-6} to 10^{-7} ms^{-1}) in the liquid, while olivine and clinopyroxene would sink with a velocity in the range of 10^{-3} to 10^{-5} ms^{-1}. Similar results are given considering a normal mid-ocean ridge basalt (NMORB) melt composition of Gale et al. (2013). This shows that intermittent convection could provoke the formation of cyclic layers by gravity settling. However, floating of plagioclase would then lead to cumulates only containing olivine and clinopyroxene with small amounts of interstitial plagioclase. The floating plagioclase would be expected to form anorthositic layers at the top of a magma reservoir which, as the olivine-clinopyroxene layers mentioned before, we do not observe in our sections. Moreover, taking grain size as a key parameter in Stoke's law into account leads to the assumption that clear coarsening of all phases toward the layer bases should be observed if the crystals uniformly settled down in a magma chamber. This is not the case (except for layer 2), which further suggests that crystal settling from a melt-rich magma is not the dominant layer-forming process.

5.2.3. Gravitational Sorting by Density Currents

As described in the previous section, crystal settling would lead to clear trends in both the modal proportions and the grain size distribution of each layer. Those could, however, be obscured during layer formation if the gravitational forces are overprinted by dynamic processes. Considering that a given magma lens crystallizes first at its margins and roof, highly crystalline parts from the roof or margins of the magma reservoir may become unstable and slump downward (Figure 13a). The concept of density currents resulting from this mechanism and forming modal layers was first proposed by Irvine (1980b). Irvine et al. (1998) then applied the same concept to modal layer formation in the Skaergaard intrusion in Greenland, and Vukmanovic et al. (2018) recently illustrated it in details. Since evidence for density currents is mostly observed in dykes and sills (Namur et al., 2015), they may also occur in the lower oceanic crust. Similar to submarine turbidites, crystals will be sorted in such a current by density and grain size (Irvine et al., 1998), leading to both modal and grain size layering (Figure 13a, $t = 1$). As shown above, plagioclase should float in a basaltic magma and is therefore expected to be expelled from the olivine-plagioclase-pyroxene-liquid system. However, consideration of other processes proposed by Irvine et al. (1998) makes clear that the mobility of plagioclase in a mafic magma—and even more in a current of crystal-laden magma—is not only controlled by density: (1) Before or during slumping of such a current, crystals might form aggregates or plagioclase can be enclosed in poikilitic clinopyroxene. Both aggregates and poikilitic grains are able to carry plagioclase downward, independently of the negative buoyancy of pure plagioclase in mafic melt. (2) Crystallization of the interstitial liquid will decrease its porosity and, therefore, can be expected to limit plagioclase buoyancy. (3) Once deposited, the yield strength of the residual liquid in the deposited layer will rapidly increase during stagnation (Murase & McBirney, 1973), hampering crystal movement within the current. (4) In case that plagioclase buoyancy overcomes the yield strength, ongoing deposition of density currents will also prevent plagioclase floatation. Additionally, it remains possible that granular plagioclase crystallized in situ after deposition of a density current.

The structure of the outcrop in Wadi Somerah (Figure 11) indicates that layers formed by a dynamic process: Although the layering appears nearly horizontal and sub-parallel from the southern point of view (Figure 11c), looking onto the western flank of the outcrop reveals highly disturbed layers with sedimentary structures (Figure 11a). This appearance can be explained by post-cumulus shear strain deforming the cumulates. Structural maps of the Oman ophiolite (Nicolas et al., 2000) reveal E-W oriented lineations in the gabbros of this region, meaning that the lineation would be perpendicular to the western outcrop face. However, field measurements would be required to develop these ideas further. Discordant layers cross-cutting each other (Figure 11b) may, however, be an indicator for slumping currents of crystal-laden magma, eroding underlying layers while moving downward.

Our petrological data suggest (except for the base of layer 2) only weak inter-phase compositional correlations (Figures 4 and 9) and are consistent with a scenario where crystals of slightly different compositions become re-sorted and form a cumulate with limited homogeneity in terms of major and minor element distributions. Trace elements also imply that there are no internal systematics whether or not the top of a layer is more fractionated than its base (Figure 10). Korenaga and Kelemen (1997) argue that density currents (or other concepts for layer formation requiring thermal gradients, such as oscillatory nucleation or double-diffusive convection) are not applicable to the modal layers in their samples due to the temperature of the system being buffered by the large-scale thermal evolution beneath the ridge. In this kind of thermally buffered system, they assume slow cooling of <1°C/kyr and thermal gradients of less than 1°C from the margin to the core of a melt sill, which raises the question whether crystallization occurs preferentially at the margins of a lens. These conditions may indeed be applicable to the gabbroic sills of the MTZ. However, the outcrop in Wadi Somerah is located in the middle of the layered gabbro sequence. Maclennan et al. (2005) modeled the thermal evolution beneath a ridge for the scenarios of both a gabbro glacier and a hybrid model combining features of subsiding crystal mush and in situ crystallization. They have shown that in both cases the middle of the lower crust is cooler than the MTZ on-axis. Applied to our samples from the mid-lower crust in Wadi Somerah, we therefore assume that they might have been subjected to lower temperatures and less thermal buffering than the samples from the MTZ investigated by Kelemen et al. (1997). The sub-solidus cooling rates estimated for Wadi Somerah indicate cooling of about $\log[dT/dt] = -2.21 \pm 0.7°C\text{yr}^{-1}$, being also faster than the very slow cooling assumed by Korenaga and Kelemen (1997), at least in the sub-solidus. It might therefore be possible that crystallization preferentially occurred at the margins of a melt lens.

Once the crystals have formed along the margins of a magma chamber, a topographic gradient is required for the crystal mush to slump down. Pallister and Hopson (1981), who already observed cross bedding and slump structures, found rare evidence for steep floor slopes during crystal accumulation. However, they cite Brown (1956) among others, who considered an angle of 15° being the maximum angle of repose for ultramafic cumulates of the Rum intrusion. We do not know the geometry of the magma reservoir where the samples from Wadi Somerah crystallized. Nonetheless, from the floor to the wall of such a reservoir, the increasing slope must have exceeded a critical angle of repose at some point where slumping of previously crystallized material might have been initialized. Slumping crystal-laden magma currents could benefit from slightly dipping chamber floors that might extend their run out distances.

In terms of rock fabrics, density currents would align minerals along a linear fabric parallel to the magmatic flow. Although indicators such as aligned and elongated olivine crystals are observed in the field, the degree of lineation obtained by EBSD is relatively weak in Wadi Somerah and is in some cases superimposed by planar fabrics, possibly caused by compaction in response to deposition by a current. Interpreting these fabrics, however, requires consideration of dynamic conditions in an assumed density current. If an already relatively solidified crystal-laden current slumps down, it is unclear whether crystal alignment occurs efficiently or is hampered due to an absence of grain mobility. Therefore, the presence of different degrees of linear fabrics does not necessarily rule out a role for density currents. Considering that field lineations are relatively homogeneous over large scales (e.g., Nicolas et al., 1988; Nicolas et al., 2000) leads to the question of whether their homogeneity is consistent with magmatic currents. In a melt lens, they are assumed to move from all sides which in turn would lead to variable lineations. However, depending on the shape of the magma lens, there might be a preferred flow direction. Assuming an elongated chamber being aligned sub-parallel to the spreading axis would be consistent with lineations being sub-perpendicular to the ridge axis at the global ophiolite scale (Nicolas et al., 2000). These workers moreover point out that on a smaller scale "a given outcrop often yields opposite shear directions" which could be formed by internal shear within magma currents slumping from opposite chamber walls.

5.2.4. Simple Shear

Beside internal shear induced by the movement of a magma current, simple shear induced by external forces (e.g., mantle movement) may occur and deform the cumulate material. Simple shear as a post-cumulus process is able to develop weak heterogeneities in a massive rock into lenticular bands (Ramsay & Graham, 1970). By studying layered gabbros in the MTZ of the Oman ophiolite, Jousselin et al. (2012) identified simple shearing, induced by lateral movement of the asthenospheric mantle, as a potentially important process for the formation of modal layering in lower oceanic crust. As Nicolas (1992) already suggested,

shearing is able to affect not only the lowermost crustal section near the MTZ but also the overlying layered gabbro sequence where they also found indicators for simple shearing. Although in some layers from Wadi Somerah olivine reveals a magmatic fabric, possibly formed by slumping currents (e.g., base of layer 5), a lineation defined by [100](010) in olivine (e.g., at the bases of layers 1 and 4) suggests a plastic deformation overprint of the highly solidified crystal mush consistent with post-cumulus shearing. Also, the deformation of layering as observed at the western flank of the outcrop in Wadi Somerah (Figure 11a) is likely to have occurred as a result of simple shear (e.g., Jousselin et al., 2012; Nicolas, 1992). Moreover, the paucity of crystal-plastic deformation cannot be seen as indicator for the absence of shear, since the presence of a small amount of interstitial melt may prevent crystal-plastic deformation (e.g., Nicolas & Ildefonse, 1996). Nonetheless, the asymmetric appearance of sharp layer bases and gradational tops in Wadi Somerah appears unlikely to have formed by externally induced simple shear, which would be expected to create olivine-rich bands without systematically gradual or sharp boundaries between neighboring layers. We therefore conclude that simple shear emphasizes heterogeneities that are already present within lower crustal rocks but that it cannot have created much of the modal layering in Wadi Somerah.

In contrast with Wadi Somerah, the contacts between millimeter-thick layers in Wadi Wariyah are symmetric with fine layers being enriched in olivine. Its proximity to the MTZ also suggests that mantle-induced shearing could have deformed the material. Moreover, olivine crystals are partially elongated, indicating significant shearing that has deformed the rocks. It is unclear, however, whether the shearing was sufficient to form the well-defined millimeter layers. According to the study of Jousselin et al. (2012), the fabrics of our sample with (010) maxima in both olivine and plagioclase, and girdles in [001] and [100], respectively, belong to the type 2 samples which represent the beginning stage of deformation. Their description of type 2 layers, "Type 2 shows weakly defined layers which can be followed over few centimeters.", however, is inconsistent with the appearance of the layering in Wadi Wariyah. From a macroscopic perspective, the layering observed here fits better the type 4 deformation in Jousselin et al.: "[...] type 4 correspond to the presence of very well-defined layers with sharp and straight limits." (Compare Figures 2 and 2d of this study with Figure 2 in Jousselin et al., 2012). However, the linear fabrics defined by Jousselin et al. (2012) for type 4 gabbros are defined by well-pronounced maxima in both [100] and (010) of olivine and plagioclase which are less clearly pronounced in our case. The less pronounced lineations in our samples could be an effect of the sample preparation which was not always performed along the *X-Z* plane of the sample. If this is the case, simple shear might have been a major process to drive the formation of layering in Wadi Wariyah.

5.2.5. Diffusion-Controlled Nucleation and Ostwald Ripening

Millimeter-scale modal bands like those observed in Wadi Wariyah can be formed under specific conditions at crystallization fronts in a cooling system, that is, at the top of a crystal mush (McBirney & Noyes, 1979): Elements diffuse through the melt toward growing crystals, and the diffusion timescale therefore increases with increasing distance from the interface, that is, the crystallization front. This may lead to a trend of increasing compatible element concentration with distance from the interface, which can ultimately provoke mineral supersaturation a certain distance ahead of the crystallization front. A new layer of crystals thus nucleates in this region of supersaturation that is separated from the underlying crystallization front, and the diffusive exchange between solid and liquid starts again (see Figure 13b, $t = 2$ for details). The potential of this process to form rhythmic layering, compare Liesegang banding, was experimentally demonstrated in saline solutions by McBirney and Noyes (1979) and Fisher and Lasaga (1981). They concluded that their experimental results could be applied to any crystallizing system and therefore could be a plausible explanation for millimeter-scale Liesegang bands. McBirney and Noyes (1979) pointed out that this process is also able to take place in magmatic systems when cooling and crystallization are faster than diffusion and thereby enable the cyclical formation of new layers. The cooling rates estimated here are calculated for a sub-solidus regime. Therefore, we cannot state whether cooling in the supersolidus also occurred atypically fast. If that was the case, mass diffusion potentially was not able to keep pace with heat diffusion leading to cyclic nucleation of olivine. This is contradictory to conclusions of Korenaga and Kelemen (1997) who excluded cyclical nucleation as layer-forming process within the MTZ due to the very slow cooling of less than 1°C/kyr buffered by the large-scale mid-ocean ridge thermal evolution. Our data which show mineral compositions with only small variations—except for layer 6—could be consistent with the cyclical nucleation model. However, the observed outlier in terms of Mg#s in olivine and clinopyroxene in layer 6 is difficult to
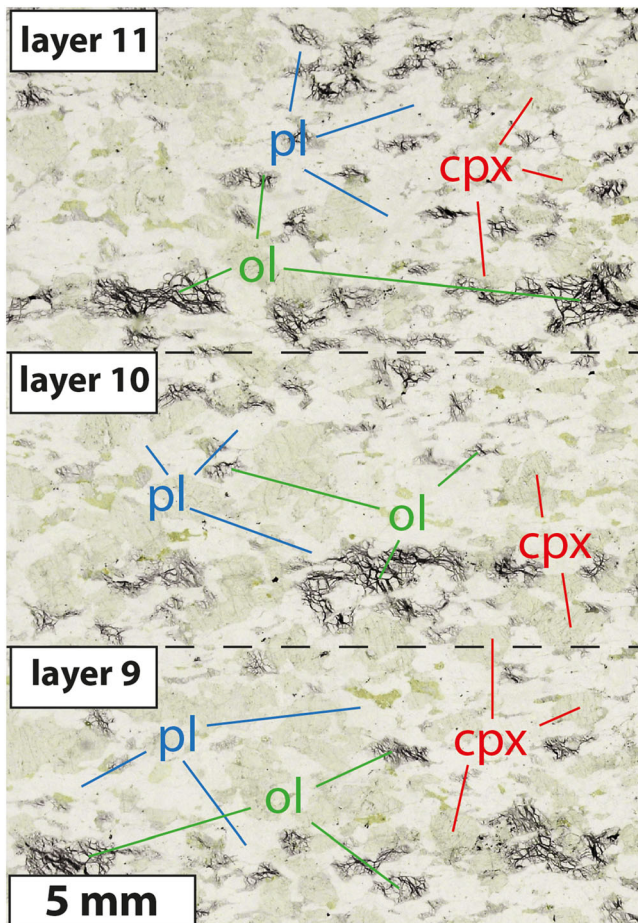
Figure 12. Thin-section photograph of sample OM10-War_DS1 from Wadi Wariyah covering the upper three fine layers. Note diffuse bands with increased olivine abundance and the olivine grains being coarser within these bands than in the regions depleted in olivine. See text for further discussion.

integrate into the proposed model. There is no textural evidence for a late stage intrusion observed. Potentially, the best explanation is a change in melt composition by a small melt influx, although it is unclear why surrounding layers are unaffected.

While our data can only give indirect evidence for the possibility of cyclical nucleation, we found evidence for the process of Ostwald ripening that was proposed by Boudreau (1995) to explain fine layering in silicate rocks: Due to their greater reactive surface in relation to their volume, smaller crystals have a higher solubility than larger ones (e.g., Boudreau, 1995). Larger crystals, that is, crystals that nucleated earlier, will therefore grow faster on the expense of smaller grains in their proximity (Figure 13c). In the sample from Wadi Wariyah we see that the olivines in the olivine-rich bands are significantly larger than those in the olivine-poor bands (Figure 12). If initial nucleation of olivine was heterogeneous (e.g., cyclical nucleation as suggested above), the heterogeneous grain size distribution between olivine-rich and olivine-poor bands indicates that Ostwald ripening occurred and emphasized initial heterogeneities in olivine nucleation forming significant millimeter-scaled differences in olivine abundance and its grain size.

5.3. Cooling Rates—Implications for Deep Hydrothermal Cooling

Both the Ca-in-olivine and the Mg-in-plagioclase geospeedometers indicate that the material from Wadi Wariyah, which formed near the MTZ, cooled up to 100 times faster in the sub-solidus regime than the mid lower crustal gabbros from Wadi Somerah. This is a counterintuitive and remarkable observation which strongly contrasts with the decreasing cooling rates down section calculated by Coogan et al. (2002) in the Nakhl-Rustaq massif of the Samail ophiolite and by Faak et al. (2015) at the EPR. The fast cooling of up to 120°C/kyr in Wadi Wariyah appears to be consistent with results from VanTongeren et al. (2008) who also calculated cooling rates in the range of up to 50°C/kyr close to the MTZ. We estimated much slower cooling ($\log[\mathrm{d}T/\mathrm{d}t] = -2.21°C \pm 0.7°C\,\mathrm{yr}^{-1}$) in the mid-level gabbros from Wadi Somerah where VanTongeren et al. found the cooling being faster than at the MTZ. However, significant differences in the approach (i.e., high resolution rim-core-rim diffusion profiles in our study, core/rim analyses averaged per thin-section in VanTongeren et al.) make the comparability of the two studies difficult.

Unexpected features of the cooling rates from Wadi Wariyah indicate that these results have to be handled with caution. Mg-in-plagioclase and Ca-in-olivine give similar and consistent results. However, it is questionable whether these reflect an undisturbed sub-solidus cooling or if the cooling has undergone late stage perturbations. Several processes appear plausible to explain the fast cooling close to the MTZ and in our sample from Wadi Wariyah in particular. Nicolas et al. (1994) and Ildefonse et al. (1995) have shown that active mantle upwelling has also affected the lowermost gabbros from the Samail ophiolite. If the upwelling leads to an efficient transport of the MTZ gabbros away from the ridge axis, gabbros from Wadi Wariyah, that is, close to the MTZ, can be assumed to cross isotherms and therefore cool faster than the mid-level gabbros from Wadi Somerah which might be less affected by active mantle upwelling.

Deep hydrothermal circulation that can efficiently transport heat away from the system (e.g., Zihlmann et al., 2018) could also be a potential explanation for the fast cooling of the lowermost gabbros. Hydrothermal circulation at high temperatures in Wadi Wariyah is supported by observations in a well-studied outcrop ~300 m south of the locality where our fine-layered sample was taken: This outcrop of layered gabbros is characterized by a complex system of hydrothermal veins containing brown pargasitic amphibole and green magnesio-hornblende which have formed under high to very high temperatures (850°C and 1030° C; Bosch, 2004; Wolff, 2013). Very high Cl contents in hastingsites and pargasites within these veins (up to
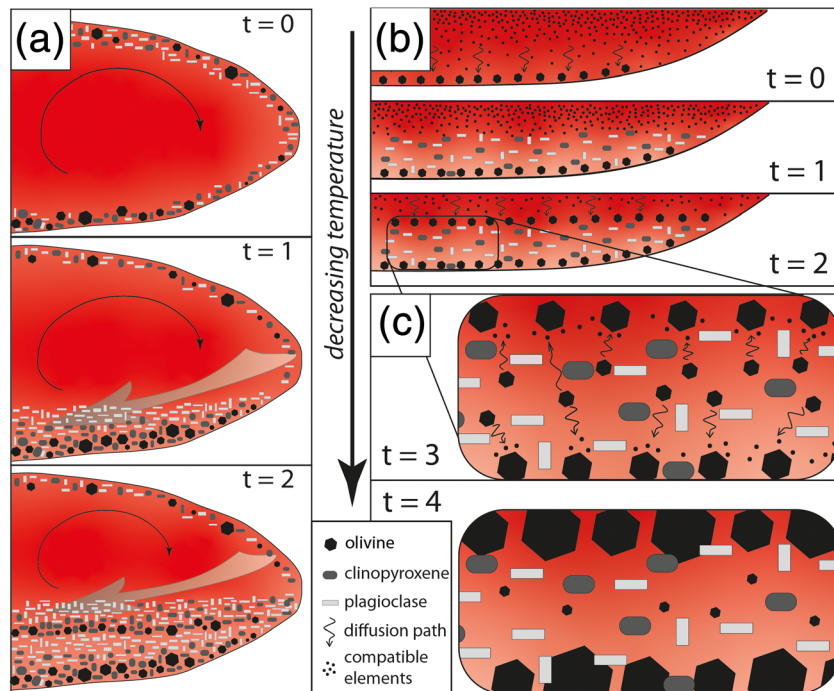
Figure 13. Igneous layer-forming processes being in agreement with our data from Wadi Somerah and Wadi Wariyah. (a) Close-up into an active melt sill showing schematically the process of density currents forming modal layering as we propose for Wadi Somerah resulting in decimeter-scale layering. Black thin arrows indicate possible convection cells; gray arrows mark slumping path of a density current. See text for details. (b) Close-up into a fast-cooled melt sill where millimeter-scale layers form due to oscillatory nucleation. Small black dots symbolize the abundance of compatible elements; thin black arrows mark their diffusion paths toward the crystallization front. See text for details. (c) Zoom into millimeter-layer formed by the process in (b). Ostwald ripening leads to coarsening of larger crystals; smaller crystals dissolve in the melt due to their higher reactive surface emphasizing modal heterogeneities. Small black dots symbolize the abundance of compatible elements diffusing from small to larger grains, as indicated by the black arrows. See text for details. Black polygones represent olivine, dark gray ellipses clinopyroxene, and light gray bars plagioclase grains. $T = x$ in every figure gives relative point in time of the sequence.

5 wt%, Currin et al., 2018) provide evidence for the presence of highly saline, seawater-derived fluids at depth. Evidence for deep hydrothermal activity at high and very high temperatures in layered gabbros from fast-spreading systems has been reported in several studies (Bosch, 2004; Garrido et al., 2001; Koepke et al., 2014; Nozaka et al., 2016). Coogan et al. (2006) outlined that hydrothermal activity is channeled to focused fluid flow zones, hence not affecting the entire crust homogeneously. It seems plausible that the sample from Wadi Wariyah represents a horizon where efficient hydrothermal cooling was enhanced, leading to higher cooling rates. In contrast, other stratigraphically higher regions were possibly less affected by focused cooling, as recorded in the Wadi Somerah section.

Further observations from the Wadi Wariyah indicate that the gabbros have been affected not only by hydrothermal fluids but also by some late stage intrusive events. A large wehrlite intrusion regarded as typical late stage event close to the locality where our sample was taken could have re-heated the surrounding solidified gabbro. Further evidence for a re-heating event are late stage gabbroic veins in the outcrop where also high-temperature hydrothermal activity was described (e.g., Bosch, 2004; Wolff, 2013). The angular shape of those veins indicates that the host rock they intruded was already highly solidified. Re-heating, either by a wehrlite intrusion or by gabbroic veins, could have led to a temporarily increased Ca or Mg solubility in olivine and plagioclase, respectively. Fast cooling, as expected after the re-heating of a relatively small volume, would record the very high Ca and Mg concentrations in both phases. Alternatively, our sample could represent a part of a large late-stage intrusion that itself cooled very quickly after entering the host rock and therefore preserved high Ca and Mg contents in olivine and plagioclase, respectively. The latter alternatives appear the most plausible, taking the presence of late stage intrusions and the generally very complex

geological environment in Wadi Wariyah into account (Figure 1b). The hypothesis mentioned above clearly reflect scenarios which are untypical for "normal" lower gabbros in the Oman ophiolite, implying that the investigated sample is not representative for typical lower, layered gabbros in Oman. However, validating these models is impossible with the data we obtained. Nonetheless, we would like to emphasize that while the high cooling rates estimated for Wadi Wariyah may not be representative for the lowermost oceanic crust as a whole, they do demonstrate that lower crustal rocks locally can cool very rapidly in some circumstances.

6. Conclusions

We sampled two short sequences of layered gabbros from the plutonic oceanic crust of the Oman ophiolite with a high spatial resolution. One sequence from Wadi Somerah sampled layered gabbros with decimeter-scale modal layering from the mid of the lower crust, while another from Wadi Wariyah sampled gabbros from about 100 m above the MTZ representing millimeter-scale modal layering at the base of the crust. The two sequences show significant differences in terms of layer properties, mineral compositions, micro-structural features, and cooling rates. While layering in the mid-lower crustal sequence (285 cm total length) is characterized by decimeter-scale modal layers with sharp base contacts and gradually decreasing olivine contents up section, the sample from the base of the crust (70-mm total length) shows alternating millimeter-scale layers with highly variable olivine contents.

Comparisons with layered intrusions suggest that the formation of the decimeter-scale layering in the mid-lower oceanic crust from Wadi Somerah could have initially formed by deposition from density currents of crystal-laden magma that had previously crystallized at the margins of a magma reservoir before slumping downward to its floor. In this model, density-triggered phase segregation occurs during the slumping, leading to an enrichment of dense olivine and clinopyroxene at layer bases and an enrichment of more buoyant plagioclase above (Figure 13a). The dynamics within such a current might prevent clear trends in grain size and phase density within a layer, as would be expected in an environment of undisturbed crystal settling (cf., Stoke's law). The millimeter-scale layering at the crustal base from Wadi Wariyah is unlikely to have formed in a similar environment. Although it is difficult to find clear evidence for any specific layer-forming process, a possible explanation could be the formation of Liesegang bands during relatively fast cooling and periodic supersaturation of compatible elements at the distance from the crystallization front at which diffusive transport cannot keep pace with the cooling (Figure 13b). Growth of large crystals at the expense of smaller ones during crystal aging is indicated by the larger size of olivine grains within the olivine-enriched layers and could have emphasized initial heterogeneity associated with Liesegang banding (Figure 13c). Alternatively, the millimeter-scale layering could have formed by simple shear, possibly induced by the convecting upper mantle close to the MTZ. Post-cumulus deformation might have affected both profiles, as it is a global feature of the Oman ophiolite, and potentially accentuated previously formed modal layering. Indicators of plastic deformation in Wadi Somerah support this assumption.

Cooling rates up to 100 times higher close to the MTZ than in the mid-layered gabbros appear not to be representative for the lowermost oceanic crust as a whole but most likely are a result of late stage re-heating events followed by relatively fast cooling and leading to local anomalies in the cooling of the oceanic crust.

Data Availability Statement

The data obtained for this study are available on the FAIR-aligned PANGAEA repository (https://doi.org/10.1594/PANGAEA.914266 for EPMA, cooling rates, and EBSD results and https://doi.org/10.1594/PANGAEA.914260 for LA-ICP-MS results and https://doi.org/10.1594/PANGAEA.914257 for petrographic results).

References

Alabaster, T., Pearce, J. A., & Malpas, J. (1982). The volcanic stratigraphy and petrogenesis of the Oman ophiolite complex. *Contributions to Mineralogy and Petrology*, *81*(3), 168–183. https://doi.org/10.1007/BF00371294

Bosch, D. (2004). Deep and high-temperature hydrothermal circulation in the Oman ophiolite—Petrological and isotopic evidence. *Journal of Petrology*, *45*(6), 1181–1208. https://doi.org/10.1093/petrology/egh010

Boudier, F., Nicolas, A., & Ildefonse, B. (1996). Magma chambers in the Oman ophiolite: Fed from the top and the bottom. *Earth and Planetary Science Letters*, *144*(1–2), 239–250. https://doi.org/10.1016/0012-821X(96)00167-7

Boudreau, A. (1995). Crystal aging and the formation of fine-scale igneous layering. *Mineralogy and Petrology*, *54*(1–2), 55–69. https://doi.org/10.1007/BF01162758

Brown, G. M. (1956). The layered ultrabasic rocks of Rhum, Inner Hebrides. *Philosophical Transactions of the Royal Society of London. Series B, Biological Sciences*, 1–53. https://doi.org/10.1098/rstb.1956.0011

Browning, P. (1984). Cryptic variation within the cumulate sequence of the Oman ophiolite: Magma chamber depth and petrological implications. *Geological Society, London, Special Publications*, *13*(1), 71–82. https://doi.org/10.1144/gsl.Sp.1984.013.01.07

Buck, W. R. (2000). *Can downward flow of dense cumulate slurry through mushy upper gabbros produce lower gabbros at a fast-spreading center?* (pp. 121–128). Boulder, CO: Special Papers - Geological Society of America.

Bunge, H. J., & Esling, C. (1982). Quantitative texture analysis. *Deutsche Gesellschaft fur Metallkunde, v+ 551, 24 x 17 cm, illustrated DM 168. 00*.

Cannat, M., & Casey, J. F. (1995). An ultramafic lift at the Mid-Atlantic Ridge: Successive stages of magmatism in serpentinized peridotites from the 15°N region. In R. L. M. Vissers & A. Nicolas (Eds.), *Mantle and Lower Crust Exposed in Oceanic Ridges and in Ophiolites* (pp. 5–34). Dordrecht: Kluwer Academic. https://doi.org/10.1007/978-94-015-8585-9_2

Chakraborty, S. (1997). Rates and mechanisms of Fe-Mg interdiffusion in olivine at 980°–1300° C. *Journal of Geophysical Research*, *102*(B6), 12,317–12,331. https://doi.org/10.1029/97JB00208

Cherniak, D. J., & Liang, Y. (2012). Ti diffusion in natural pyroxene. *Geochimica et Cosmochimica Acta*, *98*, 31–47. https://doi.org/10.1016/j.gca.2012.09.021

Coogan, L. A., Hain, A., Stahl, S., & Chakraborty, S. (2005). Experimental determination of the diffusion coefficient for calcium in olivine between 900°C and 1500°C. *Geochimica et Cosmochimica Acta*, *69*(14), 3683–3694. https://doi.org/10.1016/j.gca.2005.03.002

Coogan, L. A., Howard, K. A., Gillis, K. M., Bickle, M. J., Chapman, H., Boyce, A. J., et al. (2006). Chemical and thermal constraints on focussed fluid flow in the lower oceanic crust. *American Journal of Science*, *306*(6), 389–427. https://doi.org/10.2475/06.2006.01

Coogan, L. A., Jenkin, G. R. T., & Wilson, R. N. (2002). Constraining the cooling rate of the lower oceanic crust: A new approach applied to the Oman ophiolite. *Earth and Planetary Science Letters*, *199*(1–2), 127–146. https://doi.org/10.1016/S0012-821X(02)00554-X

Coogan, L. A., Jenkin, G. R. T., & Wilson, R. N. (2007). Contrasting cooling rates in the lower oceanic crust at fast- and slow-spreading ridges revealed by geospeedometry. *Journal of Petrology*, *48*(11), 2211–2231. https://doi.org/10.1093/petrology/egm057

Currin, A., Wolff, E. P., Koepke, J., Almeev, R., Zhang, C., Zihlmann, B., et al. (2018). Chlorine-rich amphibole in deep layered gabbros as evidence for brine/rock interaction in the lower oceanic crust: A case study from the Wadi Wariyah, Samail Ophiolite Sultanate of Oman. *Lithos*, *323*, 125–136. https://doi.org/10.1016/j.lithos.2018.09.015

Dalton, J. A., & Lane, S. J. (1996). Electron microprobe analysis of Ca in olivine close to grain boundaries: The problem of secondary X-ray fluorescence. *American Mineralogist*, *81*(1–2), 194–201. https://doi.org/10.2138/am-1996-1-224

Detrick, R. S., Buhl, P., Vera, E., Mutter, J., Orcutt, J., Madsen, J., & Brocher, T. (1987). Multichannel seismic imaging of a crustal magma chamber along the East Pacific Rise. *Nature*, *326*(6108), 35–41. https://doi.org/10.1038/326035a0

Dimanov, A., & Sautter, V. (2000). "Average" interdiffusion of (Fe, Mn)-Mg in natural diopside. *European Journal of Mineralogy*, *12*(4), 749–760. https://doi.org/10.1127/0935-1221/2000/0012-0749

Dodson, M. (1986). Closure profiles in cooling systems. *Paper Presented at the Materials Science Forum*, *7*, 145–154. https://doi.org/10.4028/www.scientific.net/MSF.7.145

Faak, K., Chakraborty, S., & Coogan, L. A. (2013). Mg in plagioclase: Experimental calibration of a new geothermometer and diffusion coefficients. *Geochimica et Cosmochimica Acta*, *123*, 195–217. https://doi.org/10.1016/j.gca.2013.05.009

Faak, K., Coogan, L. A., & Chakraborty, S. (2014). A new Mg-in-plagioclase geospeedometer for the determination of cooling rates of mafic rocks. *Geochimica et Cosmochimica Acta*, *140*, 691–707. https://doi.org/10.1016/j.gca.2014.06.005

Faak, K., Coogan, L. A., & Chakraborty, S. (2015). Near conductive cooling rates in the upper-plutonic section of crust formed at the East Pacific Rise. *Earth and Planetary Science Letters*, *423*, 36–47. https://doi.org/10.1016/j.epsl.2015.04.025

Feig, S., Koepke, J., & Snow, J. (2006). Effect of water on tholeiitic basalt phase equilibria: An experimental study under oxidizing conditions. *Contributions to Mineralogy and Petrology*, *152*, 611–638. https://doi.org/10.1007/s00410-006-0123-2

Fisher, G. W., & Lasaga, A. C. (1981). Irreversible thermodynamics in petrology. *Reviews in Mineralogy*, *8*.

France, L., Ildefonse, B., & Koepke, J. (2009). Interactions between magma and the hydrothermal system in the Oman ophiolite and in IODP hole 1256D: Fossilisation of a dynamic melt lens at fast spreading ridges. *Geochemistry, Geophysics, Geosystems*, *10*, Q10O19. https://doi.org/10.1029/2009GC002652

Gaetani, G. A., Grove, T. L., & Bryan, W. B. (1993). The influence of water on the petrogenesis of subductionrelated igneous rocks. *Nature*, *365*(6444), 332–334. https://doi.org/10.1038/365332a0

Gale, A., Dalton, C. A., Langmuir, C. H., Su, Y., & Schiling, J. (2013). The mean composition of ocean ridge basalts. *Geochemistry, Geophysics, Geosystems*, *14*, 489–518. https://doi.org/10.1029/2012GC004334

Garbe-Schonberg, D., & Muller, S. (2014). Nano-particulate pressed powder tablets for LA-ICP-MS. *Journal of Analytical Atomic Spectrometry*, *29*(6), 990–1000. https://doi.org/10.1039/c4ja00007b

Garrido, C. J., Kelemen, P. B., & Hirth, G. (2001). Variation of cooling rate with depth in lower crust formed at an oceanic spreading ridge: Plagioclase crystal size distributions in gabbros from the Oman ophiolite. *Geochemistry, Geophysics, Geosystems*, *2*, 1041. https://doi.org/10.1029/2000GC000136

Gess, M., John, B. E., Cheadle, M. J., Brown, T. C., Swapp, S., & Gee, J. S. (2018). Questioning the Penrose Paradigm: Insights from in-situ gabbroic lower ocean crust at Pito Deep. Paper Presented at the AGU Fall Meeting Abstracts.

Gillis, K. M., Snow, J. E., Klaus, A., Abe, N., Adriao, A. B., Akizawa, N., et al. (2014). Primitive layered gabbros from fast-spreading lower oceanic crust. *Nature*, *505*(7482), 204–207. https://doi.org/10.1038/nature12778

Giordano, D., Potuzak, M., Romano, C., Dingwell, D., & Nowak, M. (2008). Viscosity and glass transition temperature of hydrous melts in the system CaAl$_2$Si$_2$O$_8$–CaMgSi$_2$O$_6$. *Chemical Geology*, *256*(3–4), 203–215. https://doi.org/10.1016/j.chemgeo.2008.06.027

Goodenough, K. M., Thomas, R. J., Styles, M. T., Schofield, D. I., & MacLeod, C. J. (2014). Records of ocean growth and destruction in the Oman-UAE ophiolite. *Elements*, *10*(2), 109–114. https://doi.org/10.2113/gselements.10.2.109

Henstock, T. J., Woods, A. W., & White, R. S. (1993). The accretion of oceanic crust by episodic sill intrusion. *Journal of Geophysical Research*, *98*(B3), 4143–4161. https://doi.org/10.1029/92JB02661

Ildefonse, B., Billiau, S., & Nicolas, A. (1995). A detailed study of mantle flow away from diapirs in the Oman ophiolite. In *Mantle and Lower Crust Exposed in Oceanic Ridges and in Ophiolites* (pp. 163–177). Dordrecht: Springer.

Irvine, T. (1980b). Magmatic density currents and cumulus processes. *American Journal of Science*, *280*, 1–58.

Irvine, T. N. (1974). *Petrology of the Duke Island ultramafic complex, Southeastern Alaska* (Vol. 138). Boulder, CO: Geological Society of America.

Irvine, T. N., Andersen, J. C. O., & Brooks, C. K. (1998). Included blocks (and blocks within blocks) in the Skaergaard intrusion: Geologic relations and the origins of rhythmic modally graded layers. *Geological Society of America Bulletin*, *110*(11), 1398–1447. https://doi.org/10.1130/0016-7606(1998)110<1398:ibabwb>2.3.co;2

Jansen, M., Lissenberg, C., Klaver, M., de Graaff, S., Koornneef, J., Smeets, R., et al. (2018). Isotopic variation in Semail Ophiolite lower crust reveals crustal-level melt aggregatio. *Geochemical Perspectives Letters*, *8*, 37–42. https://doi.org/10.7185/geochemlet.1827

Jousselin, D., Morales, L. F. G., Nicolle, M., & Stephant, A. (2012). Gabbro layering induced by simple shear in the Oman ophiolite Moho transition zone. *Earth and Planetary Science Letters*, *331–332*, 55–66. https://doi.org/10.1016/j.epsl.2012.02.022

Juteau, T., Beurrier, M., Dahl, R., & Nehlig, P. (1988). Segmentation at a fossil spreading axis: The plutonic sequence of the Wadi Haymiliyah area (Haylayn Block, Sumail Nappe, Oman). *Tectonophysics*, *151*(1–4), 167–197. https://doi.org/10.1016/0040-1951(88)90245-4

Kelemen, P. B., Koga, K., & Shimizu, N. (1997). Geochemistry of gabbro sills in the crust-mantle transition zone of the Oman ophiolite: Implications for the origin of the oceanic lower crust. *Earth and Planetary Science Letters*, *146*(3–4), 475–488. https://doi.org/10.1016/S0012-821X(96)00235-X

Koepke, J., Berndt, J., Horn, I., Fahle, J., & Wolff, P. E. (2014). Partial melting of oceanic gabbro triggered by propagating water-rich fluids: A prime example from the Oman ophiolite. In H. R. Rollinson, M. P. Searle, I. A. Abbasi, A. Al-Lazki, M. H. Al-Kindi (Eds.), *Tectonic Evolution of the Oman Mountains* (Vol. 392, pp. 187–204). London: Geological Society of London, Special Publication.

Koepke, J., Schoenborn, S., Oelze, M., Wittmann, H., Feig, S., Hellebrand, E., et al. (2009). Petrogenesis of crustal wehrlites in the Oman ophiolite: Experiments and natural rocks. *Geochemistry, Geophysics, Geosystems*, *10*, Q10002. https://doi.org/10.1029/2009GC002488

Koga, K. T., Kelemen, P. B., & Shimizu, N. (2001). Petrogenesis of the crust-mantle transition zone and the origin of lower crustal wehrlite in the Oman ophiolite. *Geochemistry, Geophysics, Geosystems*, *2*. https://doi.org/10.1029/2000GC000132

Korenaga, J., & Kelemen, P. B. (1997). Origin of gabbro sills in the Moho transition zone of the Oman ophiolite: Implications for magma transport in the oceanic lower crust. *Journal of Geophysical Research*, *102*(B12), 27,729–27,749. https://doi.org/10.1029/97JB02604

Le Mee, L., Girardeau, J., & Monnier, C. (2004). Mantle segmentation along the Oman ophiolite fossil mid-ocean ridge. *Nature*, *432*(7014), 167–172. https://doi.org/10.1038/nature03075

Lippard, S. J., Shelton, A. W., & Gass, I. G. (1986). *The ophiolite of Northern Oman* (Vol. 11). Oxford: Blackwell Scientific Publ.

Lissenberg, C. J., MacLeod, C. J., Howard, K. A., & Godard, M. (2013). Pervasive reactive melt migration through fast-spreading lower oceanic crust (Hess Deep, equatorial Pacific Ocean). *Earth and Planetary Science Letters*, *361*, 436–447. https://doi.org/10.1016/j.epsl.2012.11.012

Maclennan, J., Hulme, T., & Singh, S. C. (2005). Cooling of the lower oceanic crust. *Geology*, *33*, 357–360.

MacLeod, C. J., Johan Lissenberg, C., & Bibby, L. E. (2013). "Moist MORB" axial magmatism in the Oman ophiolite: The evidence against a mid-ocean ridge origin. *Geology*, *41*(4), 459–462. https://doi.org/10.1130/g33904.1

MacLeod, C. J., & Rothery, D. A. (1992). Ridge axial segmentation in the Oman ophiolite: Evidence from along-strike variations in the sheeted dyke complex. In L. M. Parson, B. J. Murton, & P. Browning (Eds.), *Ophiolites and their Modern Oceanic Analogues* (Vol. 60, pp. 39–63). London: Geological Society Special Publication.

Mainprice, D., Bachmann, F., Hielscher, R., & Schaeben, H. (2015). Descriptive tools for the analysis of texture projects with large datasets using MTEX: Strength, symmetry and components. *Geological Society, London, Special Publications*, *409*(1), 251–271. https://doi.org/10.1144/sp409.8

McBirney, A. R., & Noyes, R. M. (1979). Crystallization and layering of the Skaergaard intrusion. *Journal of Petrology*, *20*(3), 487–554. https://doi.org/10.1093/petrology/20.3.487

McDonough, W. F., & Sun, S.-S. (1995). The composition of the earth. *Chemical Geology*, *120*(3–4), 223–253. https://doi.org/10.1016/0009-2541(94)00140-4

Mock, D., Neave, D. A., Müller, S., Garbe-Schönberg, C.-D., Namur, O., Ildefonse, B., Koepke, J. (2020a). Major element compositions of olivine, clinopyroxene and plagioclase, cooling rates and corresponding closure temperatures calculated by Ca in olivine and Mg in plagioclase, and textural properties from Wadi Somerah and Wadi Wariyah Oman, PANGAEA, https://doi.org/10.1594/PANGAEA.914266

Mock, D., Neave, D. A., Müller, S., Garbe-Schönberg, C.-D., Namur, O., Ildefonse, B., Koepke, J. (2020b). Trace element compositions in clinopyroxene and plagioclase, and crystallization temperature estimated after Sun and Liang (2017) for Wadi Somerah Oman, PANGAEA, https://doi.org/10.1594/PANGAEA.914260

Morse, S. (1984). Cation diffusion in plagioclase feldspar. *Science*, *225*(4661), 504–505. https://doi.org/10.1126/science.225.4661.504

Müller, T., Koepke, J., Garbe-Schönberg, C. D., Dietrich, M., Bauer, U., & Wolff, P. B. (2017). Anatomy of a frozen axial melt lens from a fast-spreading paleo-ridge (Wadi Gideah, Oman ophiolite). *Lithos*, *272–273*, 31–45. https://doi.org/10.1016/j.lithos.2016.11.022

Murase, T., & McBirney, A. R. (1973). Properties of some common igneous rocks and their melts at high temperatures. *Geological Society of America Bulletin*, *84*(11), 3563–3592. https://doi.org/10.1130/0016-7606(1973)84<3563:POSCIR>2.0.CO;2

Namur, O., Abily, B., Boudreau, A. E., Blanchette, F., Bush, J. W. M., Ceuleneer, G., et al. (2015). Igneous layering in basaltic magma chambers. In *Layered Intrusions* (pp. 75–152). Dordrecht: Springer.

Namur, O., Charlier, B., Toplis, M. J., Higgins, M. D., Liégeois, J.-P., & Vander Auwera, J. (2010). Crystallization sequence and magma chamber processes in the ferrobasaltic Sept Iles layered intrusion, Canada. *Journal of Petrology*, *51*(6), 1203–1236. https://doi.org/10.1093/petrology/egq016

Naslund, H. R., & McBirney, A. R. (1996). Mechanisms of formation of igenous layering. In R. G. Cawthorn (Ed.), *Layered Intrusions* (pp. 1–43). Amsterdam: Elsevier. https://doi.org/10.1016/S0167-2894(96)80003-0

Nicolas, A. (1989). *Structures of Ophiolites and Dynamics of Oceanic Lithosphere*. Dordrecht: Kluwer. https://doi.org/10.1007/978-94-009-2374-4

Nicolas, A. (1992). Kinematics in magmatic rocks with special reference to gabbros. *Journal of Petrology*, *33*(4), 891–915. https://doi.org/10.1093/petrology/33.4.891

Nicolas, A., Boudier, F., & Ildefonse, B. (1994). Evidence from the Oman ophiolite for active mantle upwelling beneath a fast-spreading ridge. *Nature*, *370*(6484), 51–53. https://doi.org/10.1038/370051a0

Nicolas, A., Boudier, F., Ildefonse, B., & Ball, E. (2000). Accretion of Oman and United Arab Emirates ophiolite—Discussion of a new structural map. *Marine Geophysical Researches*, *21*(3/4), 147–180. https://doi.org/10.1023/A:1026769727917

Nicolas, A., & Ildefonse, B. (1996). Flow mechanism and viscosity in basaltic magma chambers. *Geophysical Research Letters*, *23*(16), 2013–2016. https://doi.org/10.1029/96GL02073

Nicolas, A., Mainprice, D., & Boudier, F. (2003). High temperature seawater circulation throughout crust of oceanic ridges. A model derived from the Oman ophiolite. *Journal of Geophysical Research*, *108*, 2371. https://doi.org/10.1029/2002JB002094

Nicolas, A., Reuber, I., & Benn, K. (1988). A new magma chamber model based on structural studies in the Oman ophiolite. *Tectonophysics*, *151*(1–4), 87–105. https://doi.org/10.1016/0040-1951(88)90242-9

Nozaka, T., Meyer, R., Wintsch, R. P., & Wathen, B. (2016). Hydrothermal spinel, corundum and diaspore in lower oceanic crustal troctolites from the Hess Deep Rift. *Contributions to Mineralogy and Petrology*, *171*(6), 53. https://doi.org/10.1007/s00410-016-1266-4

Onorato, P., Hopper, R., Yinnon, H., Uhlmann, D. R., Taylor, L., Garrison, J., & Hunter, R. (1981). Solute partitioning under continuous cooling conditions as a cooling rate indicator. *Journal of Geophysical Research*, *86*(B10), 9511–9518. https://doi.org/10.1029/JB086iB10p09511

Pallister, J. S., & Gregory, R. T. (1983). Composition of the Samail Ocean crust. *Geology*, *11*(11), 638–642. https://doi.org/10.1130/0091-7613(1983)11<638:COTSOC>2.0.CO;2

Pallister, J. S., & Hopson, C. A. (1981). Samail Ophiolite plutonic suite: Field relations, phase variation, cryptic variation and layering, and a model of a spreading ridge magma chamber. *Journal of Geophysical Research*, *86*(B4), 2593–2644. https://doi.org/10.1029/JB086iB04p02593

Pearce, J. A., Alabaster, T., Shelton, A., & Searle, M. P. (1981). The Oman ophiolite as a Cretaceous arc-basin complex: Evidence and implications. *Philosophical Transactions of the Royal Society of London Series A, Mathematical and Physical Sciences*, *300*(1454), 299–317. https://doi.org/10.1098/rsta.1981.0066

Perk, N. W., Coogan, L. A., Karson, J. A., Klein, E. M., & Hanna, H. D. (2007). Petrology and geochemistry of primitive lower oceanic crust from Pito Deep: Implications for the accretion of the lower crust at the Southern East Pacific Rise. *Contributions to Mineralogy and Petrology*, *154*(5), 575–590. https://doi.org/10.1007/s00410-007-0210-z

Phipps Morgan, J. P., & Chen, Y. J. (1993). The genesis of oceanic crust: Magma injection, hydrothermal circulation, and crustal rlow. *Journal of Geophysical Research*, *98*(B4), 6283–6297. https://doi.org/10.1029/92JB02650

Pouchou, J. L., & Pichoir, F. (1991). Quantitative analysis of homogeneous or stratified microvolumes applying the model "PAP". In K. F. J. Heinrich, & D. E. Newbury (Eds.), *Electron probe quantification* (pp. 31–75). New York: Plenum Press. https://doi.org/10.1007/978-1-4899-2617-3_4

Quick, J. E., & Denlinger, R. P. (1993). Ductile deformation and the origin of layered gabbro in ophiolites. *Journal of Geophysical Research*, *98*(B8), 14,015–14,027. https://doi.org/10.1029/93JB00698

Ramsay, J., & Graham, R. (1970). Strain variation in shear belts. *Canadian Journal of Earth Sciences*, *7*(3), 786–813. https://doi.org/10.1139/e70-078

Rioux, M., Bowring, S., Kelemen, P., Gordon, S., Dudas, F., & Miller, R. (2012). Rapid crustal accretion and magma assimilation in the Oman-UAE ophiolite: High precision U-Pb zircon geochronology of the gabbroic crust. *Journal of Geophysical Research*, *117*, B07201. https://doi.org/10.1029/2012JB009273

Rioux, M., Bowring, S., Kelemen, P., Gordon, S., Miller, R., & Dudas, F. (2013). Tectonic development of the Samail ophiolite: High-precision U-Pb zircon geochronology and Sm-Nd isotopic constraints on crustal growth and emplacement. *Journal of Geophysical Research: Solid Earth*, *118*, 2085–2101. https://doi.org/10.1002/jgrb.50139

Satsukawa, T., Ildefonse, B., Mainprice, D., Morales, L. F. G., Michibayashi, K., & Barou, F. (2013). A database of plagioclase crystal preferred orientations (CPO) and microstructures—Implications for CPO origin, strength, symmetry and seismic anisotropy in gabbroic rocks. *Solid Earth*, *4*(2), 511–542. https://doi.org/10.5194/se-4-511-2013

Shejwalkar, A., & Coogan, L. A. (2013). Experimental calibration of the roles of temperature and composition in the Ca-in-olivine geothermometer at 0.1MPa. *Lithos*, *177*, 54–60. https://doi.org/10.1016/j.lithos.2013.06.013

Sparks, R. S., Huppert, H. E., Koyaguchi, T., & Hallworth, M. A. (1993). Origin of modal and rhythmic igneous layering by sedimentation in a convecting magma chamber. *Nature*, *361*(6409), 246–249. https://doi.org/10.1038/361246a0

Sun, C., & Liang, Y. (2017). A REE-in-plagioclase–clinopyroxene thermometer for crustal rocks. *Contributions to Mineralogy and Petrology*, *172*(4), 24. https://doi.org/10.1007/s00410-016-1326-9

Tamura, A., & Arai, S. (2006). Harzburgite–dunite–orthopyroxenite suite as a record of supra-subduction zone setting for the Oman ophiolite mantle. *Lithos*, *90*(1–2), 43–56. https://doi.org/10.1016/j.lithos.2005.12.012

Tilton, G. R., Hopson, C. A., & Wright, J. E. (1981). Uranium-lead isotopic ages of the Samail Ophiolite, Oman, with applications to Tethyan ocean ridge tectonics. *Journal of Geophysical Research*, *86*(B4), 2763–2775. https://doi.org/10.1029/JB086iB04p02763

Ueki, K., & Iwamori, H. (2016). Density and seismic velocity of hydrous melts under crustal and upper mantle conditions. *Geochemistry, Geosystems*, *17*, 1799–1814. https://doi.org/10.1002/2015GC006242

VanTongeren, J. A., Kelemen, P. B., & Hanghøj, K. (2008). Cooling rates in the lower crust of the Oman ophiolite: Ca in olivine, revisited. *Earth and Planetary Science Letters*, *267*(1–2), 69–82. https://doi.org/10.1016/j.epsl.2007.11.034

Vera, E. E., Mutter, J. C., Buhl, P., Orcutt, J. A., Harding, A. J., Kappus, M. E., et al. (1990). The structure of 0-my to 0.2-my old oceanic crust at 9°N on the East Pacific Rise from expanded spread profiles. *Journal of Geophysical Research*, *95*(B10), 15,529–15,556. https://doi.org/10.1029/JB095iB10p15529

Vukmanovic, Z., Holness, M., Monks, K., & Andersen, J. Ø. (2018). The Skaergaard trough layering: Sedimentation in a convecting magma chamber. *Contributions to Mineralogy and Petrology*, *173*(5), 43. https://doi.org/10.1007/s00410-018-1466-1

Wager, L. R., & Brown, G. M. (1968). *Layered Igneous Rocks*. Edinburgh and London: Oliver and Boyd.

Warren, C. J., Parrish, R. R., Waters, D. J., & Searle, M. P. (2005). Dating the geologic history of Oman's Semail ophiolite: Insights from U-Pb geochronology. *Contributions to Mineralogy and Petrology*, *150*(4), 403–422. https://doi.org/10.1007/s00410-005-0028-5

Wolff, P. E. (2013). Hydrothermal Circulation From Very High to Low Temperatures in the Lower Oceanic Crust—Evidence from Layered Gabbros from the Oman Ophiolite and From Partial Melting Experiments on Oceanic Gabbros. (PhD). University of Hannover

Yamasaki, T., Maeda, J., & Mizuta, T. (2006). Geochemical evidence in clinopyroxenes from gabbroic sequence for two distinct magmatisms in the Oman ophiolite. *Earth and Planetary Science Letters*, *251*(1–2), 52–65. https://doi.org/10.1016/j.epsl.2006.08.027

Zihlmann, B., Müller, S., Coggon, R. M., Koepke, J., Garbe-Schönberg, D., & Teagle, D. A. H. (2018). Hydrothermal fault zones in the lower oceanic crust: An example from Wadi Gideah, Samail ophiolite, Oman. *Lithos*, *323*, 103–124. https://doi.org/10.1016/j.lithos.2018.09.008

References From the Supporting Information

Abily, B., Ceuleneer, G., & Launeau, P. (2011). Synmagmatic normal faulting in the lower oceanic crust: Evidence from the Oman ophiolite. *Geology*, *39*(4), 391–394. https://doi.org/10.1130/g31652.1

Boudreau, A. (1987). Pattern formation during crystallization and the formation of fine-scale layering. In *Origins of Igneous Layering* (pp. 453–471). Dordrecht: Springer.

Boudreau, A. (1999). Fluid fluxing of cumulates: The JM reef and associated rocks of the Stillwater Complex, Montana. *Journal of Petrology*, *40*(5), 755–772. https://doi.org/10.1093/petroj/40.5.755

Boycott, A. (1920). Sedimentation of blood corpuscles. *Nature*, *104*(2621), 532–532. https://doi.org/10.1038/104532b0

Brown, P., & Farmer, D. (1971). Size-graded layering in the Imilik gabbro, East Greenland. *Geological Magazine*, *108*(6), 465–476. https://doi.org/10.1017/S0016756800056661

Dick, H. J., & Sinton, J. M. (1979). Compositional layering in alpine peridotites: Evidence for pressure solution creep in the mantle. *The Journal of Geology*, *87*(4), 403–416. https://doi.org/10.1086/628428

Ferguson, J., & Pulvertaft, T. (1963). Contrasted styles of igneous layering in the Gardar province of South Greenland. *Special Papers - Mineralogical Society of America*, *1*, 10–21.

Garbe-Schoenberg, D. (1993). Simultaneous determination of 37 trace-elements in 28 international rock standards by ICP-MS. *Geostandards Newsletter*, *17*(1), 81–97. https://doi.org/10.1111/j.1751-908X.1993.tb00122.x

Gorring, M. L., & Naslund, H. (1995). Geochemical reversals within the lower 100 m of the Palisades sill, New Jersey. *Contributions to Mineralogy and Petrology*, *119*(2–3), 263–276. https://doi.org/10.1007/BF00307286

Govindaraju, K. (1995). 1995 working values with confidence limits for twenty-six CRPG, ANRT and IWG-GIT geostandards. *Geostandards Newsletter*, *19*, 1–32. https://doi.org/10.1111/j.1751-908X.1995.tb00164.x

Hawkes, D. (1967). Order of abundant crystal nucleation in a natural magma. *Geological Magazine*, *104*(5), 473–486. https://doi.org/10.1017/S0016756800049219

Higgins, M. D. (1991). The origin of laminated and massive anorthosite, Sept Iles layered intrusion, Quebec, Canada. *Contributions to Mineralogy and Petrology*, *106*(3), 340–354. https://doi.org/10.1007/BF00324562

Higgins, M. D. (2011). Textural coarsening in igneous rocks. *International Geology Review*, *53*(3–4), 354–376. https://doi.org/10.1080/00206814.2010.496177

Hoffer, A. (1965). Seismic control of layering in intrusions. *American Mineralogist: Journal of Earth and Planetary Materials*, *50*(7–8), 1125–1128.

Huppert, H. E., & Sparks, R. S. J. (1981). The fluid dynamics of a basaltic magma chamber replenished by influx of hot, dense ultrabasic magma. *Contributions to Mineralogy and Petrology*, *75*(3), 279–289. https://doi.org/10.1007/BF01166768

Imai, N., Terashima, S., Itoh, S., & Ando, A. (1995). 1994 compilation of analytical data for minor and trace elements in seventeen GSJ geochemical reference samples,"Igneous rock series". *Geostandards Newsletter*, *19*(2), 135–213. https://doi.org/10.1111/j.1751-908X.1995.tb00158.x

Irvine, N. (1980a). Magmatic infiltration metasomatism, double diffusive fractional crystallization, and adcumulus growth in the Muskox intrusion and other layered intrusions. In *Physics of magmatic processes* (pp. 325–384). Princeton, NJ: Princeton University Press. https://doi.org/10.1515/9781400854493.325

Jackson, E. (1961). Primary Textures and Mineral Associations in the Ultramafic Zone of the Stillwater Complex, Montana: US Geol. Survey Prof. Paper 358, 106 p. 1963, Chromium. *23rd Session*, Sec, 1, 135–140.

Jochum, K. P., Stoll, B., Herwig, K., Willbold, M., Hofmann, A. W., Amini, M., et al. (2006). MPI-DING reference glasses for in situ microanalysis: New reference values for element concentrations and isotope ratios. *Geochemistry, Geophysics, Geosystems*, *7*, Q02008. https://doi.org/10.1029/2005GC001060

Jochum, K. P., Weis, U., Schwager, B., Stoll, B., Wilson, S. A., Haug, G. H., et al. (2016). Reference values following ISO guidelines for frequently requested rock reference materials. *Geostandards and Geoanalytical Research*, *40*(3), 333–350. https://doi.org/10.1111/j.1751-908X.2015.00392.x

Jochum, K. P., Willbold, M., Raczek, I., Stoll, B., & Herwig, K. (2005). Chemical characterisation of the USGS reference glasses GSA-1G, GSC-1G, GSD-1G, GSE-1G using EPMA, ID-TIMS, ID-ICP-MS and LA-ICP-MS. *Geostandards and Geoanalytical Research*, *29*(3), 285–302. https://doi.org/10.1111/j.1751-908X.2005.tb00901.x

Korzhinskii, D. (1968). The theory of metasomatic zoning. *Mineralium Deposita*, *3*(3), 222–231. https://doi.org/10.1007/bf00207435

Lesher, C., & Walker, D. (1988). Cumulate maturation and melt migration in a temperature gradient. *Journal of Geophysical Research*, *93*(B9), 10,295–10,311. https://doi.org/10.1029/JB093iB09p10295

Liesegang, R. (1896). Ueber einige eigenschaften von gallerten. *Naturwissenschaftliche Wochenschrift*, *10*(30), 353–362.

Lipin, B. R. (1993). Pressure increases, the formation of chromite seams, and the development of the ultramafic series in the Stillwater Complex, Montana. *Journal of Petrology*, *34*(5), 955–976. https://doi.org/10.1093/petrology/34.5.955

Marsh, B. D. (1989). On convective style and vigor in sheet-like magma chambers. *Journal of Petrology*, *30*(3), 479–530. https://doi.org/10.1093/petrology/30.3.479

McBirney, A. R. (1987). Constitutional zone refining of layered intrusions. In *Origins of Igneous Layering* (pp. 437–452). Dordrecht: Springer.

McBirney, A. R., & Nakamura, Y. (1974). Immiscibility in late-stage magmas of the Skaergaard intrusion. *Carnegie Institution of Washington Yearbook*, *73*, 348–352.

Moore, A. C. (1973). Studies of igneous and tectonic textures and layering in the rocks of the Gosse Pile intrusion, Central Australia. *Journal of Petrology*, *14*(1), 49–79. https://doi.org/10.1093/petrology/14.1.49

Naslund, H., Turner, P., & Keith, D. (1991). Crystallization and Layer Formation in the Middle Zone of the Skaergaard Intmsion.

Petersen, J. S. (1987). Solidification contraction: Another approach to cumulus processes and the origin of igneous layering. In *Origins of Igneous Layering* (pp. 505–526). Dordrecht: Springer.

Sparks, R. S. J., Huppert, H. E., Kerr, R., McKenzie, D., & Tait, S. R. (1985). Postcumulus processes in layered intrusions. *Geological Magazine*, *122*(5), 555–568. https://doi.org/10.1017/S0016756800035470

Ulmer, G. (1969). Experimental investigations of chromite spinels. In *Magmatic Ore Deposits. Symp. Econ. Geol. Monograph* (Vol. 4, pp. 114–131). Michigan: Economic Geology Publishing Company.

Wilson, J. R., Menuge, J. F., Pedersen, S., & Engell-Sørensen, O. (1987). The southern part of the Fongen-Hyllingen layered mafic complex, Norway: Emplacement and crystallization of compositionally stratified magma. In *Origins of Igneous Layering* (pp. 145–184). Dordrecht: Springer.